Revision 2: The origin of Ti-oxide minerals below and within the eastern Athabasca Basin, Canada

Erin E. Adlakha[1,2], Keiko Hattori[2], Mitchell J. Kerr[1] and Brandon M. Boucher[3]

[1]Department of Geology, Saint Mary's University, 923 Robie St., Halifax, Nova Scotia, Canada, B3H3C3

[2]Department of Earth and Environmental Sciences, University of Ottawa, 25 Templeton Dr., Ottawa, Ontario, Canada, K1N6N5

[3]Department of Earth Sciences, University of New Brunswick, 2 Bailey Drive, Fredericton, New Brunswick, Canada, E3B5A3

Corresponding author: erin.adlakha@smu.ca

Abstract

Titanium oxide minerals along the P2 fault in the eastern Athabasca Basin are characterized to constrain their origin and the geological history of the area. Two types of rutile are recognized in the basement rocks. Early rutile is disseminated in graphitic metapelite and quartzite and formed during regional metamorphism and post-metamorphic hydrothermal activity. Late rutile occurs as a needle-like alteration product of mica and likely formed during retrogression of the basement. In graphitic metapelite, early rutile commonly occurs with an assemblage of oxy-dravite, quartz, graphite, zircon, pyrite, biotite and muscovite. In quartzite, rutile occurs with quartz, sillimanite, and zircon. Metamorphic rutile is characterized by high Nb/Ta ratios (up to 47) with high concentrations of U (up to 126 ppm) and V^{4+} (up to 1.44 wt%; V valance calculated from EPMA data). Hydrothermal rutile contains distinctly low Nb/Ta (as low as 4.80) with high Ta (≤3050 ppm), and relatively low V (as V^{3+}; as low as 0.02 wt.%) and U (as low as 9.06 ppm), reflecting fluids in reduced oxidation conditions. Anatase forms small anhedral (rarely coarse and euhedral) grains in the basal sandstones and altered basement rocks. In sandstones, anatase occurs with the late diagenetic mineral assemblage, whereas in basement rocks it commonly occurs with the clay-sized minerals related to uranium mineralization. In both rocks, anatase likely formed through the dissolution of rutile and/or other Ti-bearing minerals. Anatase is characterized by variably high Fe (up to 0.99 wt.%; possibly contributed by hematite micro- or nanoinclusions) and U (up to 180 ppm). The mineral assemblages and composition of anatase suggest its protracted crystallization from relatively low temperature, oxidizing, acidic, uraniferous fluids from the sandstones during late diagenesis and hydrothermal activity. Therefore, the occurrence of anatase records the incursion of basin fluids into the basement, and the interaction of basement rocks with fluids responsible for the formation of the McArthur River uranium deposit. The results of this study confirm that Ti-oxides are useful in unraveling the geological history of an area that underwent prolonged hydrothermal activity.

Keywords: rutile, anatase, P2 fault, McArthur River, unconformity-type uranium deposits, alteration

Introduction

The Paleoproterozoic Athabasca Basin, and crystalline basement rocks, experienced multiple alteration events including the hydrothermal activity related to the formation of world-class unconformity-type uranium deposits. Many petrological studies over the past 40 years aim to unravel the paragenesis of the area (e.g., Hoeve and Sibbald 1977; Kotzer and Kyser 1995; Fayek and Kyser 1997; Alexandre et al. 2005, 2009, 2012; Cloutier et al. 2011; Reid et al. 2014;

Adlakha and Hattori 2015, 2016), in order to evaluate the nature of uranium mineralization and its timing with respect to the geological evolution of the area. This information is critical to assess the conditions and geological environments for the formation of these giant uranium deposits. Although Ti-oxide minerals are noted in these rocks (e.g., Kotzer and Kyser 1995; Fayek and Kyser 1997; Alexandre et al. 2005, 2009; Cloutier et al. 2009, 2010, 2011), there have been no detailed studies of the minerals.

Titanium-oxide minerals form different polymorphs (rutile, anatase, brookite) and accommodate a wide variety of minor elements, reflecting their crystallizing environments (e.g., Meinhold 2010). Although the P-T conditions for the polymorph's stability are not well constrained, considering contradicting interpretations (Osborn, 1953; Dachille et al., 1968, 1969; Jameison and Olinger, 1969; Gribb and Banfield 1997; Zhang and Banfield 1999, 2000; Ranade et al. 2002; Navrotsky 2003; Levchenko et al. 2006; Smith et al. 2009; Mei et al. 2014; Curnan and Kitchin 2015, Plavsa et al. 2018), it is generally accepted that rutile is more stable than anatase, and the polymorphic transition of anatase to rutile is favourable over rutile to anatase under most conditions (Dachille et al. 1968). This is supported by observations of rutile in both high and low temperature environments, and anatase in only low temperature environments. Regardless of the polymorph stability, it is apparent that rutile is the most common Ti-oxide polymorph in Earth's crust (Meinhold et al. 2010). It occurs in metamorphic rocks of various facies ranging from greenschist to granulite and eclogite; as detrital and authigenic grains in sedimentary rocks; in igneous rocks, particularly evolved granitic rocks and pegmatite (Černý 1989); and in hydrothermally altered rocks and metallic mineral deposits including Cu-Mo porphyry deposits, volcanogenic massive sulphide deposits and orogenic Au deposits (e.g., Schandl et al. 1990; Urban et al. 1992; Scott 2005; Scott and Radford 2007; Rabbia et al. 2009;

Agangi et al. 2019). Once rutile is crystallized, it is usually resistant to hydrothermal alteration owing to the insoluble nature of Ti in most aqueous fluids (e.g., Ayers and Watson 1993). Anatase is indicative of low temperature, aqueous environments, such as diagenetic systems (Smith et al. 2009), along with less common brookite. Anatase is commonly reported as an authigenic mineral in siliciclastic sedimentary rocks (e.g., Morad and Aldahan 1986; Morad 1986; Pe-Piper et al. 2011), and likely forms through the breakdown of detrital titaniferous minerals, such as Ti-rich oxides, biotite, and titanite. Considering these properties, Ti-oxide minerals may be useful in petrologic studies of altered rocks, such as those common in the Athabasca Basin.

This paper describes the occurrence, polymorphs, and chemical composition of Ti-oxide in well-characterized samples of metasedimentary basement and Athabasca sandstone along the P2 fault, which is the major structure in the eastern basin and hosts all ore bodies of the exceptionally high-grade McArthur River uranium deposit (Fig. 1). The P2 fault is not only an important structural control for mineralization, but also served as a fluid pathway during uriniferous hydrothermal activity (Adlakha and Hattori 2015, 2016; Adlakha et al. 2017). The study integrates micro-analytical data using a field emission scanning electron microscope (SEM) for detailed textural analysis, Raman spectroscopy to identify Ti-oxide polymorphs, electron probe microanalysis (EPMA) to quantify major element abundances, and laser ablation inductively coupled plasma mass spectroscopy (LA-ICP-MS) for trace element abundances. The data are used to evaluate the origin and relative timing of Ti-oxide crystallization. This information is used to constrain the paragenetic history of this economically important area.

Geological Background

Regional Geology

The basement below the eastern Athabasca Basin belongs to the Wollaston supergroup, which consists of Paleoproterozoic metasedimentary rocks, including metapelite, graphitic metapelite, meta-arkose, calc-silicate, and quartzite, intruded by anatexic granitic lenses (Fig. 1). Regional metamorphism of the Wollaston supergroup during the 1.92 to 1.80 Ga Trans-Hudson Orogen reached upper amphibolite to lower granulite facies conditions (Annesley et al. 2005; Corrigan et al. 2009). The origin of quartzite, which forms topographic highs at the unconformity, is debated. The rocks are considered to have formed during regional metamorphism of quartz-rich sedimentary rocks, or hydrothermal activity after the peak metamorphism prior to the deposition of the Athabasca Basin (Annesley and Millar 2011; Card 2012; Card 2013). Chemical weathering of the basement is recorded as a paleo-weathering profile along the unconformity (Macdonald 1985; Adlakha et al. 2013).

The eastern Athabasca Basin is composed of ~500 m of fluvial quartz dominated (~99%) conglomeratic sandstones, consisting of four major sequences: the lower Read formation, and the Manitou Falls formations B, C and D (Fig. 1b). The sandstones contain minor hematite, dickite-kaolinite, illite and Sr-Ca-SO_4^{2-}-rich aluminum phosphate sulfate (APS) minerals (e.g., Kotzer and Kyser 1995; Gaboreau 2007). The regional diagenetic minerals (primarily dickite with hematite) are overprinted by illite, chlorite, magnesio-foitite (alkali-deficient Mg-rich tourmaline), and LREE-P rich APS minerals near the vicinity of uranium deposits and basement structures (Kotzer and Kyser 1995; Gaboreau et al. 2007; Jefferson et al. 2007).

Local Geology

The P2 fault is a 13 km long reverse structure (~050, 45-60 SE) along graphitic metapelite of the Wollaston supergroup, which originated as a ductile structure during the Trans-Hudson Orogen. The fault underwent brittle reactivations during and after deposition of the unconformably overlying sandstones of the Athabasca Basin (e.g., McGill 1993; Hajnal et al. 2010). Vertical movement along the P2 fault is responsible for displacement of the unconformity by up to 80 m and the fault extends into the lower sandstones as splays and fractures (McGill 1993).

Extensive alteration occurs along the P2 fault zone in the basement, including the areas of mineralization and barren of mineralization (e.g., McGill 1993; Adlakha and Hattori 2015, 2016). The least altered rocks found far outside the fault zone and below the paleo-regolith consist mainly of biotite ± garnet and sillimanite gneisses and coarse-grained to pegmatitic granite lenses consisting of predominately quartz, plagioclase and K-feldspar ± mica. The earliest alteration of the basement fault is expressed as veins of oxy-dravite, graphite, pyrite, and quartz, which postdates the peak metamorphism and predates the deposition of the Athabasca Basin (Adlakha and Hattori 2016, Adlakha et al. 2017). The prevalent alteration along the fault is associated with uranium mineralization of the McArthur River deposit and comprises illite, sudoite (Al-Mg chlorite), magnesio-foitite and LREE-P rich APS minerals (Kotzer and Kyser 1995; Gaboreau et al. 2007; Alexandre et al. 2009; Ng et al. 2013; Adlakha and Hattori 2015, 2016). The assemblage also forms a halo around the ore bodies of the McArthur River deposit.

The McArthur River deposit comprises nine mineralized zones and three showings, which are structurally controlled by the P2 fault and unconformity (Fig. 1c; Bray et al. 2018). All ore bodies are hosted within the lowermost sandstone unit of the Athabasca Basin, with the exception of Zone 2 that is almost completely hosted within the basement rocks. The Zone 2 ore body is additionally bound by the Vertical Quartzite (VQ) fault that runs along the contact between basement quartzite and graphitic metapelite (Adlakha and Hattori 2015). The McArthur River deposit is the largest high-grade uranium deposit yet discovered in the world, with an average grade of ~7.14 % U_3O_8 in proven reserves (Bray et al. 2018). Low grade or sub-economic mineralization, including the P2 Main deposit, is found sporadically along the fault outside of the main deposit area (Fig, 1c).

Sampling and Analytical Methods

Eighteen samples were selected for this study, primarily based on the abundance of Ti-oxide minerals observed during petrographic work and to ensure representation of all areas of the P2 fault relative to the McArthur River deposit (e.g., mineralized, low-grade, apparently barren; Table 1, Fig. 1c). Sixteen samples are of the basement rocks along the fault and two are of basal conglomeratic sandstone of Read formation immediately above the unconformity (Table 1; Fig. 2).

Mineral identification, textural analysis and imaging were carried out using a petrographic microscope in both transmitted and reflected light on polished thick (~100 μm) sections, followed by a TESCAN MIRA 3 LMU Variable Pressure Schottky Field Emission SEM at Saint Mary's University, Halifax, Nova Scotia, using a working distance of 17 mm and accelerating voltage of 20 kV.

Polymorphs of Ti-oxide were distinguished using a Jobin-Yvon Horiba LabRam HR confocal laser Raman microspectrometer at Saint Mary's University, Halifax, Nova Scotia.

Phase identification used Raman shifts at 242, 449 and 614 cm^{-1} for rutile, and 199, 400, 517 and 642 cm^{-1} for anatase. Analyses were performed using a 532 nm (green) Nd-YAG laser (105 mW laser power at objective) focused through a 100x objective lens. Spectra were collected using a 600 grooves/mm grating, 50 µm confocal hole size, and Synapse 1024 x 256 pixel CCD detector. Spectra collection was performed using an acquisition duration of 10s with 3 accumulations. Frequency calibration was performed using a pure silicon wafer.

The chemical composition of Ti-oxide minerals was determined by wavelength dispersive X-ray spectrometry using a JEOL 8230 SuperProbe at the University of Ottawa, Ottawa, Ontario. The working conditions were set to an accelerating voltage of 20 kV with a 40 nA beam current focussed to a 5 µm spot size. Data collection time was 40 s with 20 s background time for all elements. Analytical standards include spinel [$(Cr,Mg,Al,Fe)_3O_4$ for AlKα, CrKα, and MgKα], Mn columbite (NbLα), ThO_2 (ThMα), zircon (ZrLα), $NiTa_2O_6$ (TaMα), rutile (TiKα), cassiterite (SnLα), $CoWO_4$ (WMα), UO_2 (UMα), powellite (MoLα), vanadinite (VKα), hematite (FeKα), tephroite (MnKα), and diopside (SiKα). Data reduction used the ZAF program. Data for FeO were recalculated as Fe_2O_3, considering Fe in rutile is usually Fe^{3+} in most environments, even in reducing conditions (e.g., Vlassopoulos et al. 1993). Detection limits are listed in Appendix Tables 1 and 2. Due to the irregular shape and small size of anatase crystals, Si and Al values were monitored for contamination by surrounding silicate minerals.

Trace element abundances were determined using a Resonetics S-155-LR 193nm Excimer laser ablation system coupled to an Agilent 7700x quadrupole ICP-MS at the University of New Brunswick, Fredericton, New Brunswick. Detailed running conditions of the LA-ICP-

MS are listed in Appendix Table 3. All grains were examined for inclusions before analysis, and time-sequence intensity graphs of the data were inspected for possible inclusions. The data were imported into IGOR Pro (Version 6.3.7, Wavemetrics Inc.) and reduction was carried out using the add-on Iolite (Version 2.5). The calibration standard NIST610 (National Institute of Standards and Technology, synthetic glass) and ratio of each isotope to counts of ^{49}Ti (using average EPMA data for Ti in Ti-oxides from each sample) were used to quantify trace element abundances. Analysis of BCR-2G (Columbia River Basalt, USGS) indicates accuracy within 10% and precision within 5% for the trace elements. Data of the same grains using LA-ICP-MS and EPMA yielded similar results for elements Nb, W, and Cr (Appendix Fig. 1). Data of V produced by LA-ICP-MS yields higher values (systematically by ~1000 ppm) than EPMA.

Results

Ti-oxide Polymorph Occurrences and Petrography

Examination of representative grains of Ti-oxide in samples using Raman spectroscopy identified two Ti-oxide polymorphs: rutile and anatase (Figs. 3a, b; Table 1). Brookite was not detected in any samples. The host rocks, mineral assemblages, and paragenesis of the Ti-oxide polymorphs are described below and illustrated in Figure 4.

Rutile occurs as a minor but common mineral in hydrothermally altered metapelite and quartzite (Table 1; Fig. 5). No rutile was observed in sandstone samples. In thin section, rutile is dark reddish-brown to opaque under transmitted light (Figs. 5a, b), and weakly-moderately reflective light grey with a faint bluish tint in reflected light. Three types of rutile are identified based on texture (Table 2). The most abundant type of rutile (Type 1) occurs as disseminated, euhedral-subhedral grains ranging from 20 to 500 µm in diameter with corroded rims and fractures (Fig. 5a). The host rocks for Type 1 rutile are mainly foliated and altered graphitic metapelite with or without cm-scale leucosomes (e.g., Fig. 2a), but it also occurs in the quartzite sample (MAC79). Type 1 rutile is distributed along all studied areas of the P2 fault, including the areas near mineralization, such as Zones 1 (samples MAC201, 203), 2 (MAC70, 79, 84, 86, 152, 441, 444), 4 (MAC420), and the low-grade P2 Main deposit (MAC98, 99), as well as unmineralized areas (MAC127, 426, 436) (Fig. 1c; Tables 1 and 2). Some metapelites show varying degrees of early silicification (e.g., Figs. 2c, d,) where large (> 1cm) patches of anhedral quartz replace metapelite. Late-stage brecciation with desilicification and alteration by light blue magnesio-foitite is common in samples from both mineralized (e.g, MAC99; Fig. 2d) and unmineralized areas (e.g. MAC436, Fig. 2e). Some metapelite samples are in contact with anatexite (> 10 cm wide) (e.g., MAC420; Fig. 2f); although the granitic lenses do not contain Ti-oxide minerals. Notably, Type 1 rutile is absent in mineralized sample MAC423 of the Zone 2 ore body, which contains a cm-wide vein of primary uraninite bordered by red hematite (Fig. 2g). Type 1 rutile does occur in sample MAC98 below the P2 Main deposit, which contains veinlets of a U-oxide phase containing high Si and Ca. This phase is similar in composition to U-Ca hydroxide reported by Fayek and Kyser (1997), which is considered to be a remobilization product of primary uraninite.

Type 1 rutile is early in all samples and commonly occurs with an assemblage of oxy-dravite, quartz, graphite, zircon, pyrite, and micas (biotite and/or muscovite; Figs. 4, 5a-c; Table 2). This assemblage occurs in veins or bands parallel with fabric of graphitic metapelite samples from all areas of the fault (apparently barren and mineralized; Fig. 1c; e.g, samples MAC84, 99, 127, 201, 420 and 436). In these samples, disseminated rutile and graphite laths occur with, and sometimes as inclusions in, sub-euhedral oxy-dravite and quartz (Figs. 5a-c). Zircon and quartz are also found as inclusions in rutile and oxy-dravite (Fig. 5a). The micas are commonly altered by chlorite. Sample MAC127 is unusual as it contains a low abundance of oxy-dravite, in addition to a Mg-mineral (possibly cordierite) that is pseudomorphed by sudoite (Fig. 5b). This Mg-mineral is likely an earlier metamorphic mineral as it occurs as inclusions in oxy-dravite and is embayed by graphite. In other metapelite samples (e.g., MAC70, 86, 98, 127, 152, 203, 441, 444), the minerals that formed together with rutile are largely replaced by later clay-sized minerals, except for quartz, pyrite, zircon, and graphite in some samples (MAC70, 86, 441, 444). Therefore, it is difficult to determine the exact minerals that formed together with rutile in these samples. In samples MAC98, 152, and 203, the only mineral preserved with rutile is quartz (Fig. 5d). In unbrecciated samples MAC152 and 203, feldspar grains are evident but pseudomorphed by fine-grained illite, whereas feldspar grains are not recognized in brecciated and intensely altered sample MAC98. In the quartzite sample (MAC79), Type 1 rutile forms subhedral to anhedral intergrowths with quartz that contains acicular sillimanite crystals (Fig. 5e). Rutile and quartz occur with muscovite that is coated by Fe-oxide (Fig. 5e). In this sample, euhedral zircon occurs as inclusions in rutile, quartz, and muscovite.

The second type (Type 2) of rutile is fine-grained and blocky. It only occurs in sample MAC98 from below the P2 Main deposit (Fig. 5f). This rutile occurs as inclusions with rounded anatase within an altered coarse-grained mineral. The mineral is pseudomorphically replaced by sudoite and dendritic to patchy anatase. The third type (Type 3) occurs as fine-grained, elongate grains along cleavage planes of chloritized (Fe-Mg chlorite) muscovite and biotite in samples MAC70, 84, 86, 127, 423, 441, and 444, which represent all areas of the fault (Figs. 1c, 5c).

Late clay-sized minerals are common in the studied samples and predominately consist of sudoite, illite, and magnesio-foitite with or without LREE-P rich APS minerals or anatase. These minerals surround and infill fractures of rutile, oxy-dravite and graphite. Magnesio-foitite forms overgrowths on intergrown oxy-dravite and rutile (Figs. 5a,c,d,f). Notably, rutile in mineralized sample MAC98 is fractured and coated by late secondary U-oxide (Fig. 5d).

Anatase is observed in samples of both sandstone and the basement (Table 2). It is opaque to translucent and brown-blue in thin section under transmitted light (Fig. 6a). Anatase is moderately reflective and grey in reflected light (Fig. 6b). It is distinguished from rutile in thin sections by texture because anatase is usually anhedral and fine-grained with irregular grain boundaries. Additionally, anatase is darker in BSE images than rutile (Fig. 5f).

Anatase occurs in sandstone samples of the basal Read formation in unmineralized (MAC430) and low grade (MAC406) areas of the P2 fault (Fig. 1c). Both sandstone samples consist of banded, fine to coarse-grained, detrital quartz with red to buff coloured interstitial clay (kaolinite-group minerals and illite), due to varying amounts of fine-grained hematite (Fig. 2h). Note that kaolinite-group minerals will be referred to simply as kaolin because polymorphs (i.e. kaolinite vs. dickite) were not in identified this study. Titanium oxides were not observed in samples of the upper sandstone units in this study (n = 5), such as those in the Manitou Falls formation.

In both sandstone samples, anatase is concentrated in the silty layers comprising detrital quartz and zircon, and authigenic minerals such as kaolin, illite, APS minerals and fine-grained red hematite (Figs. 6a,b; Table 2). Anatase grains in sandstones are typically anhedral and patchy, occurring in clusters and sometimes containing inclusions of Fe-oxide (Figs. 6b,c). The anatase grains overprint diagenetic kaolin and crosscut overgrowths of detrital quartz grains, which contain Sr and SO_4^{2-}-rich APS minerals (Fig. 6c). Anatase is in textural equilibrium with coarse-grained (~20 µm) illite, which alters earlier kaolin (Fig. 6b).

The mode of occurrence for anatase varies in basement samples (e.g., MAC98, MAC423, MAC426, MAC436) and is summarized in Table 2. In sample MAC98, anatase forms both rounded grains (< 15 µm) and dendritic to patchy growths in the altered coarse-grained mineral described above, as well as fine-grained disseminations (Fig. 5f). Based on compositional similarities, both the rounded and patchy anatase are of similar origin, likely replacements of the unidentified altered mineral (see next section on anatase composition). The disseminated anatase occurs with stringers of hematite in the matrix of sudoite and magnesio-foitite, which are overprinted by late secondary U-hydroxide. In mineralized sample MAC423, anatase occurs as irregular anhedral to lath-like disseminations in clay-sized minerals near the margin of the uraninite vein and is coated by secondary U-hydroxide (Fig. 6d). In sample MAC426, anatase forms euhedral to anhedral coarse grains (up to 100 µm). This anatase occurs as inclusions in dolomite, which is intergrown with coarse-grained and lath-like black hematite (Fig. 6a). In back-scattered electron images, some anatase grains in MAC426 contain euhedral bright cores reflecting high W and Fe content (Fig. 6a). In sample MAC436, anatase forms clusters of small (< 15 µm), and rarely coarse, anhedral grains disseminated in fine-grained magnesio-foitite with LREE-P rich APS minerals around large euhedral rutile with corroded rims (Figs. 5b, 6e,f). Both latter samples are from unmineralized portions of the P2 fault.

Major and Minor Element Composition

The composition of rutile is determined using 290 EPMA measurements from 15 samples (see Table 3 for the average values, and Appendix Table 1 for the entire dataset). All data are of Type 1 disseminated rutile, except for 5 measurements of Type 2 rutile inclusions in the altered coarse-grained mineral. Type 3 rutile is too fine-grained for accurate analysis. Type 1 rutile contains variably high Nb (up to 2.70 wt.%), Fe (up to 0.78 wt.%), V (up to 1.44 wt.%) and W (up to 0.51 wt.%) (Table 3). In individual samples, rutile grains are similar in composition (Table 3). The composition of Type 1 and 2 rutile in sample MAC98 are similar and contain exceptionally high Nb (average 3.29 wt.%; Table 3). Contents of Al, Th, Sn, U, Mo, Mn and Mg are close to, or lower than the detection limits of the instrument.

Forty-seven EPMA measurements of anatase from five samples (MAC98, 406, 426, 430, 436) indicate variably high Fe content (up to 0.99 wt.%; Table 4; Appendix Table 2 for the full dataset). These data do not include fine-grained skeletal anatase in MAC98 or lathlike anatase in MAC423 as it is commonly coated by U-oxide. Except for sample MAC426, anatase contains mostly low concentrations of impure elements compared to rutile: up to 0.55 wt.% Nb, 0.06 wt.% Cr, 0.05 wt.% W, 0.31 wt.% V, 0.10 wt.% Al, and 0.07 wt.% Si (Table 4). Most anatase grains contain low Zr (<0.13 wt.%). Contents of Mg, Mn, Mo, Sn, Ta, Th and U are below the detection limits of the EPMA. Two types of anatase were analyzed in MAC98, the early rounded inclusions and patchy replacements. The early anatase inclusions have high Fe (0.24 wt.%) and essentially no V, whereas the patchy replacement anatase is either compositionally similar or contains relatively low Fe (~0.08 wt.%) and high V (up to 0.31 wt.%). Anatase in sample

MAC426 is compositionally distinct and contains variably high Fe (up to 0.99 wt.%), W (up to 2.01 wt.%), Cr (up to 0.15 wt.%) and Zr (up to 0.36 wt.%).

Trace Element Abundances

One hundred and twenty-six measurements of rutile (Type 1) from thirteen samples and fifteen measurement of anatase from five samples using LA-ICP-MS are reported. Small number of anatase measurement is due to its small grain size. Average trace element concentrations of rutile and anatase are listed in Tables 3 and 4, respectively (see Appendix Tables 5 and 6, respectively, for full data sets).

Trace element data show that rutile contains variable Ca (up to 120 ppm), Sc (5.8 to 1050 ppm), Co (up to 102 ppm), Se (up to 170 ppm) Sn (up to 440 ppm), Hf (up to 178 ppm), Th (up to 44 ppm), and U (up to 126 ppm). Rutile contains low Mo (<33 ppm), Y (<21 ppm) and Pb (<7.4 ppm).

Anatase contains variable concentrations of Ca (up to 9760 ppm), Sn (up to 130 ppm), Hf (up to 160 ppm), Ta (up to 190 ppm), Th (up to 68.7 ppm), Pb (up to 32 ppm) and U (up to 180 ppm). Anatase contains low concentrations of Ga (<2.59 ppm), Y (<9.5 ppm), and Mo (<8.8 ppm).

Discussion

Crystal Chemistry of Ti-Oxide Minerals

Rutile consists of chains of TiO_6^{8-} octahedra that share two edges and extend parallel to the c-axis (Klein and Dutrow 2007). Adjacent octahedral chains are linked through sharing of a single O, with each O in triangular coordination with Ti. Rutile in this study shows extensive substitution of Ti with Fe, V, and Nb (Table 3). While tetravalent cations can undergo simple substitution with Ti ($M^{4+} \leftrightarrow Ti^{4+}$), non-tetravalent cations in rutile are commonly accommodated by coupled substitutions: $M^{2+} + M^{6+} \leftrightarrow 2Ti^{4+}$, $M^{3+} + M^{5+} \leftrightarrow 2Ti^{4+}$, $M^{2+} + 2M^{5+} \leftrightarrow 3Ti^{4+}$, and $2M^{3+} + 2M^{6+} \leftrightarrow 3Ti^{4+}$ (e.g., Urban et al. 1992; Scott and Radford 2007).

Previous studies indicate Fe^{2+}, Fe^{3+}, V^{3+}, and V^{4+} are compatible with rutile (e.g. Urban et al. 1992). The oxidation state of Fe and V in rutile of this study and their substitution mechanisms are evaluated using biplots (Fig. 7). The slope of Ti and V range from -1 to -½, reflecting V^{4+} substituting for Ti^{4+} in some rutile (Fig. 7a; e.g., MAC70, 84, 86, 127) and V^{3+} in others (e.g., MAC79, 98, 99, 201, 203, 420). The V and Nb contents of rutile containing V^{3+} exhibit a slope of 1 (Fig. 7b), suggesting V^{3+} is accommodated by coupled substitution with Nb^{5+} ($V^{3+} + Nb^{5+} \leftrightarrow 2Ti^{4+}$). Iron in rutile is generally considered to be Fe^{3+} (Vlassopoulos et al. 1993 and references therein). Iron and Nb in some rutile show a slope between 1 and ½, suggesting variable valence of Fe (Fig. 7c). Many rutile grains contain high Nb relative to Fe, as the data trends plot below the ½ sloped line without intersecting 0 (Fig. 7c). This is explained by coupled substitution of Nb with minor amounts of other trivalent elements, such as V^{3+}, Cr^{3+}, and Al^{3+} (Fig. 7d)

The V^{4+}-bearing rutile grains have relatively high V content, compared to V^{3+}-bearing rutile. This likely reflects the compatibility of V^{4+} over V^{3+} in rutile, considering V^{4+} has the same charge and is similar in size in 6-fold coordination (0.78 Å for V^{3+} vs. 0.72 for V^{4+}) to Ti^{4+} (0.745 Å). Except for rutile from MAC98, V^{3+}-bearing rutile contains relatively lower V and higher Fe and Nb (Fig. 7d). The compositional difference between these two rutile types may be attributed to varying fO_2, where V^{4+} is preferentially incorporated into rutile over Fe and Nb under oxidizing conditions.

Anatase, like rutile, consists of Ti in octahedral coordination with O, and O in triangular coordination with Ti. In anatase, the Ti octahedra share edges with four adjacent octahedral (Klein and Dutrow 2007). Anatase contains variably high Fe, with lesser V, Nb and W (Table 4). Vanadium and Ti in V-rich anatase of MAC98 show a correlation with a slope of -1 suggesting the occurrence of V as V^{4+} (Fig. 8a). Iron and Nb show a large scatter (Fig. 8b) Notably, anatase of MAC426 shows a broad correlation between W and Fe with a slope of 2 (Fig. 8c), suggesting Fe^{3+} and W^{6+} ($2Fe^{3+} + W^{6+} \leftrightarrow 3Ti^{4+}$). The oxidized state of Fe in anatase is also supported by abundant hematite in the samples (Figs. 4, 5f, 6a).

The majority of Fe in anatase is not charge balanced by other cations, such as Nb (Fig. 8b) and W (Fig. 8c). High Fe^{3+} may be attributed to microinclusions of hematite, which were observed in sandstone-hosted anatase. Inverse correlations between Ti and Fe with a slope of 1 for both sandstone and basement hosted anatase can be explained by contamination of the EPMA data with hematite (Fig. 8d); however, hematite inclusions were not observed in the basement anatase. It is possible these anatase contain nano-inclusions that were obvious using SEM. Alternatively, a substantial amount of OH^- may occur in the O^{2-} site of Ti-oxides to compensate the substitution of trivalent cations ($M^{3+} + OH^- \leftrightarrow Ti^{4+} + O^{2-}$; e.g., Soffer 1961, Vlassopoulos et al. 1993, Tompsett et al. 1995, Swope et al. 1995, Smyth 2006). Therefore, it is possible that OH^- may charge balance Fe^{3+}. Unfortunately, the presence of OH- is not confirmed as it is not detectable by the methods used in this study. The mechanism for high Fe^{3+} in anatase remains unresolved, but hematite microinclusions, and possibly nanoinclusions, are the most likely explanation at this point.

The Origin of Ti-oxide Minerals Along the P2 Fault

The origin of Ti-oxide phases along the P2 fault is evaluated using mineral textures, assemblages, and mineral composition.

Rutile. Three texturally distinct types of rutile occur in basement samples (Table 2; Fig. 4). Type 1 rutile in graphitic metapelite and quartzite occurs with different mineral associations, suggesting its crystallization during multiple events. Type 2 rutile is rare, occurring only in sample MAC98. Considering it is essentially identical in composition with Type 1 rutile (Table 3), the two types of rutile in this sample are considered to be of similar origin. Type 3 rutile is similar in texture to needle-like rutile in chloritized biotite laths observed in the basement rocks outside the P2 fault (Adlakha et al. 2013). The Type 3 rutile likely shares a similar origin, which is interpreted to be an alteration product of mica during retrograde metamorphism (Adlakha et al. 2013).

Textural evidence indicates that Type 1 rutile pre-dates the low temperature basinal hydrothermal activity that formed magnesio-foitite, sudoite, and illite ± uraninite (Figs. 4, 5). This is evident from the textural equilibrium between rutile and oxy-dravite, which are both surrounded by magnesio-foitite (Fig. 5a; Adlakha and Hattori 2016). In samples without oxy-dravite, fractures of rutile are filled with the late alteration minerals listed above. Both rutile and oxy-dravite must have rystallized before deposition of the Athabasca Basin considering oxy-dravite occurs as a detrital mineral in the Athabasca sandstones (Mercadier et al. 2012, Adlakha and Hattori 2016). Therefore, the possible origins of this Type 1 rutile include: i) detrital origin (pre-metamorphism of the basement), ii) crystallization during metamorphism of the basement, or iii) post-peak metamorphic hydrothermal crystallization.

A detrital origin is consistent with the rounded shape of some Type 1 rutile grains, such as those abundant in sample MAC436 (Fig. 5e). The common association of rutile in this study with other "heavy minerals" such as tourmaline and zircon (e.g., MAC99, MAC436; Figs. 5a,6e) also supports the detrital origin. If they are indeed detrital, they must have recrystallized and/or underwent Ostwalt ripening in order to achieve such large grain sizes during later metamorphism and hydrothermal activity. Their composition would have likely been modified during these later processes.

During metamorphism and hydrothermal activity, Ti is generally immobile (Ayers and Watson 1993). Therefore, both metamorphic and hydrothermal rutile forms through the breakdown or alteration of precursor Ti-bearing minerals, such as biotite, rutile, ilmenite, titanite, titaniferous magnetite, and Ti-rich amphibole (e.g., Schwartz 1958; Luvizotto and Zack 2009; Meinhold et al. 2010). Type 1 rutile of this study exhibit euhedral to ovoid disseminated grains, similar to those reported in other high-grade metamorphic rocks (e.g. Meinhold et al. 2010). However, we suggest its formation during multiple events based on its mineral association.

Rutile incorporates high-field strength elements (HFSE; Nb, Ta, Zr, Hf, U and Th), and their ratios may help constrain its origin (Bau 1996; Luvizotto and Zack 2009; Carocci et al. 2019; Pereira et al. 2019; Zeh et al. 2018; Plasva et al. 2018). For example, rutile formed from the breakdown of Ti-bearing minerals, such as biotite and ilmenite, during high grade metamorphism inherits variably high Nb/Ta ratios (Figs. 9a, b; Luvizotto and Zack 2009; Meyer et al. 2011; Stepanov and Hermann 2013). On the other hand, rutile formed from hydrothermal fluids show characteristically low Nb/Ta ratios and high Ta (Carruzzo et al. 2006; Dostal et al. 2009). The fractionation of Ta from Nb in aqueous fluids is attributed to a variety of reasons, including the availability of ligands forming soluble complexes (e.g., Bau et al. 1996), and the preferential incorporation of one element into other minerals (e.g., Dostal et al. 2000).

The Nb/Ta ratios of Type 1 rutile in this study are between 5 to 24 (average 13 ± 6, 1σ; Fig. 9a), which bracket the value for average continental crust (12.4; Fig 9b; Rudnick and Gao, 2003). The majority of samples show an inverse relationship between Nb/Ta and Ta, which is consistent with rutile in pelitic rocks that formed during high grade metamorphism (Luvizotto and Zack 2009; Meyer et al. 2011; Figs. 9a,b). Therefore, high Nb/Ta ratios of the majority of rutile grains suggest a metamorphic origin. However, some low values correspond with high Ta and do not follow the trend, suggesting a different origin. As previously mentioned, rutile with low Nb/Ta ratios and high Ta characterizes hydrothermal rutile. In addition, the low Nb/Ta rutile grains are from samples containing different mineral assemblages, including MAC99 with oxy-dravite, quartzite of MAC79, and highly altered samples MAC98, 203, and 441 (Table 2). The different mineralogy of these samples suggest that they were not formed during a single hydrothermal event. Notably, recent studies propose that the quartz-rich and tourmaline-graphite-pyrite rich rocks, similar to those that contain this rutile, are products of pre-Athabasca hydrothermal activity after the peak metamorphism of the basement (Annesley and Millar 2011; Card 2012; Adlakha and Hattori 2016).

The Zr/Hf ratios of rutile of metamorphic and hydrothermal origine may be distinct, where the former exhibits higher ratios than the latter (Fig. 9b; Luvizotto and Zack 2009; Meyer et al. 2011; Pereira et al. 2019). The Zr/Hf ratios of rutile in this study show low variability (average 18 ± 2, 1σ) and overlap with both metamorphic and hydrothermal rutile elsewhere (Fig. 9b). Considering the common occurrence of zircon in our samples, the Zr/Hf ratios of rutile in our samples are likely controlled by zircon (Figs. 5c,e).

Type 1 rutile is characterized by low Th (commonly less than the detection limit of the ICP-MS) and variably high U (9.06 to 126 ppm; Fig. 9c). This is consistant with the incompatibility of Th rutile (usually <0.5 ppm) due to its large ionic radius (Brenan et al. 1994; Klemme et al., 2005). Hexavalent U is compatible with rutile (Brenan et al. 1994) and high U is common for rutile in metapelitic rocks (Zack and Kooijman 2017). Accordingly, the rutile of a suspected metamorphic origin (i.e. those with high Nb/Ta ratios such as in MAC84, 86, 127, and 152; Fig 9a) contains relatively high U (Fig. 9c). The basement rocks below the Athabasca Basin are notably rich in U (e.g., Hecht and Cuney, 2000), and interaction of fluids with such rocks could also explain high U in rutile. Considering U is soluble as U^{6+} in oxidizing aqueous fluids, high U in hydrothermal rutile likely indicates oxidizing conditions of the fluids, whereas low U indicates reduced fluids. Interestingly, the suspected hydrothermal rutile (high Ta with low Nb/Ta ratios (e.g., MAC79, 98, 99, 203, 436 and 441) contains relatively low U, which may indicate their formation or recrystallization by fluids in reduced oxidation conditions. The formation of these rutile under reduced conditions is supported by the occurrence of V as reduced V^{3+} (e.g., MAC79, 98, 99, 203; Figs. 7a,d). Figure 9d, a biplot of the ratios of V/Nb versus Fe/V, demonstrates that rutile with V^{3+} contains high Nb and Fe, whereas rutile with high V^{4+} contains low Nb and Fe. The relative abundance of U, V, Nb, and Fe may be useful to qualitatively indicate the oxidation conditions during the formation of different generations of rutile. (Figs. 9c, d).

Anatase. Anatase of this study occurs in the hematitized basal sandstone and basement. In the sandstone samples, anatase crosscuts the early diagenetic assemblage of quartz overgrowths with kaolin and Sr-rich APS minerals, suggesting anatase crystallization during late diagenesis or early hydrothermal activity. Since the phase transformation of rutile to anatase is not thermodynamically favorable (Osborn 1953; Smith et al. 2009), we suggest that anatase crystallized through dissolution of Ti-bearing detrital minerals, such as rutile, at relatively low temperatures. Titanium is soluble in highly acidic fluids (e.g., Vikre and John, 2010; Pe-Piper et al. 2011), which prevailed during the diagenesis and subsequent uraniferous hydrothermal activity in Athabasca Basin (e.g., Kister et al. 2005). The original detrital mineralogy of the sandstones is largely affected by the diagenetic-hydrothermal assemblages and even relatively insoluble detrital minerals such as tourmaline, monazite and zircon show partial dissolution (e.g., Fayek and Kyser 1997; Gaboreau 2007; Adlakha and Hattori 2016).

Anatase in the basement occurs near uranium mineralization and in apparently barren areas (Table 1; Fig. 1c). In these samples, disseminated anatase is typically fine-grained (< 15 μm) and associated with magnesio-foitite, sudoite, illite, and overprinted by late U-hydroxide. The textural evidence suggests anatase crystallized together with magnesio-foitite, sudoite, and illite. We suggest that anatase of the basement forms from the dissolution of Ti-bearing minerals (e.g., rutile and mica), considering the occurrence of fine-grained anatase disseminated around rutile with corroded rims (Fig. 6e). Additionally, lath-like anatase near the uranium mineralization likely pseudomorph mica (Fig. 6d) and skeletal and patchy anatase overprint the unknown coarse-grained mineral (Fig. 4f). In the basement, anatase also forms subhedral-euhedral inclusions in late dolomite with coarse-grained hematite (Fig. 6a). This anatase is likely derived from the alteration of Ti-bearing minerals of the wallrock. Although veins of dolomite and quartz are found proximal to uranium deposits (e.g., Kotzer and Kyser 1995, Derome et al. 2005), this particular sample (MAC426) occurs in an apparently barren area (Fig. 1c), ~80 m below the unconformity. Considering anatase i) occurs with hematite in both sandstone and basement samples, ii) post-dates the diagenetic assemblage of the sandstones, and iii) is coeval with magnesio-foitite, sudoite and illite in the basement, we suggest the protracted crystallization of anatase in both rock types by oxidizing and acidic hydrothermal fluids from the basin shortly after diagenesis and during hydrothermal activity related to uranium mineralization (Fig. 4).

To the best of the authors' knowledge, no study has been conducted on the partitioning of elements between anatase and fluids. Based on EPMA data, anatase of this study generally contains lower concentrations of impurities than rutile, except for variably high Fe in most anatase and high Fe and W in anatase of MAC426 (Figs. 7, 9d). These data are consistent with anatase compositions reported elsewhere (e.g. Triebold et al. 2011; Plavsa et al. 2018). Considering that anatase commonly occurs with hematite (Table 1; Figs. 2g-h, 5h-i), it is unsurprising that anatase contains high Fe^{3+}. The low concentrations of other elements may reflect the relatively low temperature of anatase crystallization, as low temperatures deter incorporation of impurities. Furthermore, adjacent Ti-O octahedra in anatase share four edges compared with two in rutile (Klein and Dutrow 2007). This may restrict the substitution of large and/or highly charged cations in anatase.

Anatase of this study shows similar Nb/Ta ratios as rutile with variable Zr/Hf ratios, and contents of U and Th depend on host rock (e.g., basement vs. sandstone; Figs. 9a-c). The Nb/Ta ratios are likely inherited from precursor rutile. Sandstone-hosted anatase shows variably high Zr/Hf ratios (up to 39; open diamond markers in Fig. 9b). Since Zr and Hf are mostly hosted by zircon, they are likely transferred to anatase during the partial dissolution of detrital zircon. The Zr/Hf ratios of detrital zircon are estimated to average 37 ± 10(1σ), based on whole rock data of the Athabasca sandstones compiled by Wright et al. (2015) (n = 8418; data filtered for U = 0 to 3 ppm, Zr and Hf > 0). These whole rock ratios are similar to those of anatase in sandstones, confirming our proposed interpretation. Anatase in metapelite predominately exhibits low Zr/Hf ratios (≤ 23, filled diamond markers in Fig. 9b), similar to the basement-hosted rutile except for one grain of anatase from MAC98 with a very high value of 61. Sandstone hosted anatase contains high U (up to 181 ppm) and surprisingly very high Th contents (up to 47 ppm). High U content likely reflect the presence of U^{6+} in the oxidizing basinal fluids of the Athabasca Basin. High Th in anatase is confirmed to be in the crystal structure based on microtextures and LA-ICP-MS spectra. While high Th content in Ti-oxide is unusual, high Th is reported for authigenic rutile in sedimentary rocks elsewhere (Dunkl and von Eynatten 2009). Since sandstones generally contain high Th/U compared to mudstones, high Th in anatase may reflect a contribution from sandstones.

Implications

Titanium oxides along a major fault within and below the eastern Athabasca Basin record a protracted geological history. Early rutile in graphitic metapelite and quartzite of the basement formed through recrystallization of fine-grained detrital rutile during regional metamorphism and hydrothermal activity prior to the deposition of the Athabasca sandstones. The relative abundance of U, Fe, V, Nb and Ta of rutile discriminate rutile of different origin (e.g. metamorphic vs. hydrothermal) and qualitatively indicate oxidation conditions during its crystallization. After sedimentation and diagenesis of the sandstones, acidic basinal fluids formed anatase in sandstones and the basement at the expense of rutile and other Ti-bearing minerals. The composition of anatase in sandstone records the presence of oxidizing uraniferous basinal fluids. The presence of anatase in basement rocks records the incursion of basin fluids into the basement, marking the onset of hydrothermal activity related to the McArthur River uranium deposit. The results of this study confirm that Ti-oxides are useful in unraveling the geological history of an area that underwent prolonged hydrothermal activity.

Acknowledgements

This project was funded by Natural Resources of Canada through the Targeted Geoscience Initiative Four (TGI-4) program, a Research Affiliate Program Bursary to EEA and a grant to KH. We thank Eric G. Potter, science leader for the TGI-4 uranium ore system project, at the Geological Survey of Canada, for his continuous support. Cameco Corporation provided their logistical support for our field work at the McArthur River mine. Special thanks extend to Gerard Zaluski and Tom Kotzer, as well as Aaron Brown, Doug Adams, Remi Labelle, and Brian McGill of Cameco Corp. for their help during the field work. We thank Xiang Yang of SMU for his assistance with SEM work, and Glenn Poirier and David Diekrup of the University of Ottawa for their assistance with EPMA work. We thank Gemma Olivo (Queen's University) and an anonymous reviewer for their constructive reviews, which improved the quality of our paper. We also thank associate editor Jie Xiu for handling the manuscript.

References

Adlakha, E. E., Hattori, K., Zaluski, G., Kotzer, T., Potter, E. G., and File, O. (2013) Alteration within the basement rocks associated with the P2 fault and the McArthur River uranium deposit, Athabasca Basin. Geological Survey of Canada Open File Report, 7462, 33.

Adlakha, E. E., and Hattori, K. (2015) Compositional variation and timing of aluminum phosphate-sulfate minerals in the basement rocks along the P2 fault and in association with the McArthur River uranium deposit, Athabasca Basin, Saskatchewan, Canada. American Mineralogist, 100, 1386-1399.

Adlakha, E. E., and Hattori, K. (2016) Paragenesis and composition of tourmaline types along the P2 fault and McArthur River uranium deposit, Athabasca Basin, Canada. The Canadian Mineralogist, 54, 661-679.

Adlakha, E. E., Hattori, K., Davis, W. J., and Boucher, B. (2017) Characterizing fluids associated with the McArthur River U deposit, Canada, based on tourmaline trace element and stable (B, H) isotope compositions. Chemical Geology, 466, 417-435.

Agangi, A., Reddy, S. M., Plavsa, D., Fougerouse, D., Clark, C., Roberts, M., and Johnson, T. E. (2019) Antimony in rutile as a pathfinder for orogenic gold deposits. Ore Geology Reviews, 106, 1-11.

Alexandre, P., Kyser, K., Polito, P., and Thomas, D. (2005) Alteration mineralogy and stable isotope geochemistry of Paleoproterozoic basement-hosted unconformity-type uranium deposits in the Athabasca Basin, Canada. Economic Geology, 100, 1547-1563.

Alexandre, P., Kyser, K., and Jiricka, D. (2009) Critical geochemical and mineralogical factors for the formation of unconformity-related uranium deposits: comparison between barren and mineralized systems in the Athabasca Basin, Canada. Economic Geology, 104, 413-435.

Alexandre, P., Kyser, K., Jiricka, D., and Witt, G. (2012) Formation and evolution of the Centennial unconformity-related uranium deposit in the south-central Athabasca Basin, Canada. Economic Geology, 107, 385-400.

Annesley, I. R., Madore, C., and Portella, P. (2005) Geology and thermotectonic evolution of the western margin of the Trans-Hudson Orogen: evidence from the eastern sub-Athabasca basement, Saskatchewan. Canadian Journal of Earth Sciences, 42, 573-597.

Annesley, I. R., and Millar, R. (2011) Tourmaline-and sulfide-bearing graphitic pelitic gneisses of the Paleoproterozoic Wollaston Group, northern Saskatchewan: new insights into understanding the carbon-sulfur-boron-uranium geochemical system with implications for U/C-type uranium deposits. Proceedings of the 25th International Applied Geochemistry Symposium.

Ayers, J. C., and Watson, E. B. (1993) Rutile solubility and mobility in supercritical aqueous fluids. Contributions to Mineralogy and Petrology, 114, 321-330.

Bau, M. (1996) Controls on the fractionation of isovalent trace elements in magmatic and aqueous systems: evidence from Y/Ho, Zr/Hf, and lanthanide tetrad effect. Contributions to Mineralogy and Petrology, 123, 323-333.

Bray, L., Murdock, G. M., and Renaud, A. D. (2018) McArthur River Operation Northern Saskatchewan, Canada. National Instrument 43-101 Technical Report, 141.

Brenan, J. M., Shaw, H. F., Phinney, D. L., and Ryerson, F. J. (1994) Rutile-aqueous fluid partitioning of Nb, Ta, Hf, Zr, U and Th: implications for high field strength element depletions in island-arc basalts. Earth and Planetary Science Letters, 128, 327-339.

Card, C. D. (2012) The origins of anomalously graphitic rocks and quartzite ridges in the basement to the southeastern Athabasca Basin. Summary of Investigations, 2, 2012-2014.

Card, C. D. (2013) Altered pelitic gneisses and associated “quartzite ridges” beneath the southeastern Athabasca Basin: alteration facies and their relationship to uranium deposits along the Wollaston-Mudjatik transition. Summary of Investigations, 2, 2013-2014.

Carocci, E., Marignac, C., Cathelineau, M., Truche, L., Lecomte, A., and Pinto, F. (2019) Rutile from Panasqueira (Central Portugal): An Excellent Pathfinder for Wolframite Deposition. Minerals, 9, 9.

Carruzzo, S., Clarke, D. B., Pelrine, K. M., and MacDonald, M. A. (2006) Texture, composition, and origin of rutile in the South Mountain Batholith, Nova Scotia. The Canadian Mineralogist, 44, 715-729.

Černý, P., Chapman, R., Göd, R., Niedermayr, G., and Wise, M. A. (1989) Exsolution intergrowths of titanian ferrocolumbite and niobian rutile from the Weinebene spodumene pegmatites, Carinthia, Austria. Mineralogy and Petrology, 40, 197-206.

Cloutier, J., Kyser, K., Olivo, G. R., Alexandre, P., and Halaburda, J. (2009) The Millennium uranium deposit, Athabasca Basin, Saskatchewan, Canada: an atypical basement-hosted unconformity-related uranium deposit. Economic Geology, 104, 815-840.

Cloutier, J., Kyser, K., Olivo, G. R., and Alexandre, P. (2010) Contrasting patterns of alteration at the Wheeler River area, Athabasca Basin, Saskatchewan, Canada: Insights into the apparently uranium-barren Zone K alteration system. Economic Geology, 105, 303-324.

Cloutier, J., Kyser, K., Olivo, G. R., and Brisbin, D. (2011) Geochemical, isotopic, and geochronologic constraints on the formation of the Eagle Point basement-hosted uranium deposit, Athabasca Basin, Saskatchewan, Canada and recent remobilization of primary uraninite in secondary structures. Mineralium Deposita, 46, 35-56.

Corrigan, D., Pehrsson, S., Wodicka, N., and De Kemp, E. (2009) The Palaeoproterozoic Trans-Hudson Orogen: a prototype of modern accretionary processes. Geological Society, London, Special Publications, 327, 457-479.

Curnan, M. T., and Kitchin, J. R. (2015) Investigating the energetic ordering of stable and metastable TiO2 polymorphs using DFT+ U and hybrid functionals. The Journal of Physical Chemistry C, 119, 21060-21071.

Dachille, F., Simons, P. Y., and Roy, R. (1968) Pressure-temperature studies of anatase, brookite, rutile and TiO2-II. American Mineralogist: Journal of Earth and Planetary Materials, 53, 1929-1939.

Dachille, F., Simons, P. Y., and Roy, R. (1969) Pressure-temperature studies of anatase, brookite, rutile and TiO2 (II): A reply. American Mineralogist: Journal of Earth and Planetary Materials, 54, 1481-1482.

Derome, D., Cathelineau, M., Cuney, M., Fabre, C., Lhomme, T., and Banks, D. A. (2005) Mixing of sodic and calcic brines and uranium deposition at McArthur River, Saskatchewan, Canada: a Raman and laser-induced breakdown spectroscopic study of fluid inclusions. Economic Geology, 100, 1529-1545.

Dostal, J., and Chatterjee, A. K. (2000) Contrasting behaviour of Nb/Ta and Zr/Hf ratios in a peraluminous granitic pluton (Nova Scotia, Canada). Chemical Geology, 163, 207-218.

Dunkl, I., and von Eynatten, H. (2009) Anchizonal-hydrothermal growth and (U-Th)/He dating of rutile crystals in the sediments of Hawasina window, Oman. Geochimica et Cosmochimica Acta Supplement, 73, A314.

Fayek, M., and Kyser, T. K. (1997) Characterization of multiple fluid-flow events and rare-earth-element mobility associated with formation of unconformity-type uranium deposits in the Athabasca Basin, Saskatchewan. The Canadian Mineralogist, 35, 627-658.

Gaboreau, S., Cuney, M., Quirt, D., Beaufort, D., Patrier, P., and Mathieu, R. (2007) Significance of aluminum phosphate-sulfate minerals associated with U unconformity-type deposits: The Athabasca basin, Canada. American Mineralogist, 92, 267-280.

Gribb, A. A., and Banfield, J. F. (1997) Particle size effects on transformation kinetics and phase stability in nanocrystalline TiO2. American Mineralogist, 82, 717-728.

Hajnal, Z., White, D.J., Takacs, E., Gyorfi, I., Annesley, I.R., Wood, G., O'Dowd, C. and Nimeck, G. (2010) Application of modern 2-D and 3-D seismic-reflection techniques for uranium exploration in the Athabasca Basin. Canadian Journal of Earth Sciences, 47, 761-782.

Hecht, L., and Cuney, M. (2000) Hydrothermal alteration of monazite in the Precambrian crystalline basement of the Athabasca Basin (Saskatchewan, Canada): implications for the formation of unconformity-related uranium deposits. Mineralium Deposita, 35, 791-795.

Hoeve, J., and Sibbald, T. I. I. (1978) On the genesis of Rabbit Lake and other unconformity-type uranium deposits in northern Saskatchewan, Canada. Economic Geology, 73, 1450-1473.

Jamieson, J. C., and Olinger, B. (1969) Pressure-temperature studies of anatase, brookite rutile, and Ti02 (II): A discussion. American Mineralogist: Journal of Earth and Planetary Materials, 54, 1477-1481.

Jefferson, C. W., Thomas D. J., Gandhi, S. S., Ramaekers, P., Delaney, G., Brisbin, D., ... and Olson, R. A. (2007) Unconformity-associated uranium deposits of the Athabasca basin, Saskatchewan and Alberta; in EXTECH IV: Geology and Uranium EXploration TECHnology of the Proterozoic Athabasca Basin, Saskatchewan and Alberta. Geological Survey of Canada Bulletin, 588, 23-67.

Kister, P., Vieillard, P., Cuney, M., Quirt, D., and Laverret, E. (2005) Thermodynamic constraints on the mineralogical and fluid composition evolution in a clastic sedimentary basin: the Athabasca Basin (Saskatchewan, Canada). European Journal of Mineralogy, 17, 325-342.

Klein, C., Dutrow, B., and Dana, J. D. (2007) The 23rd edition of the manual of mineral science, 716 p. Wiley, New Jersey.

Klemme, S., Prowatke, S., Hametner, K., and Günther, D. (2005) Partitioning of trace elements between rutile and silicate melts: implications for subduction zones. Geochimica et Cosmochimica Acta, 69, 2361-2371.

Kotzer, T. G., and Kyser, T. K. (1995) Petrogenesis of the Proterozoic Athabasca Basin, northern Saskatchewan, Canada, and its relation to diagenesis, hydrothermal uranium mineralization and paleohydrogeology. Chemical Geology, 120, 45-89.

Levchenko, A. A., Li, G., Boerio-Goates, J., Woodfield, B. F., and Navrotsky, A. (2006) TiO2 stability landscape: Polymorphism, surface energy, and bound water energetics. Chemistry of Materials, 18, 6324-6332.

Luvizotto, G. L., and Zack, T. (2009) Nb and Zr behavior in rutile during high-grade metamorphism and retrogression: an example from the Ivrea–Verbano Zone. Chemical Geology, 261, 303-317.

Macdonald, C., Sibbald, T. I. I., and Petruk, W. (1985) Mineralogy and geochemistry of the sub-Athabasca regolith near Wollaston Lake. Geology of Uranium Deposits: Canadian Institute of Mining and Metallurgy Special, 32, 155-158.

McGill, B. (1993) The P2 north uranium deposit Saskatchewan, Canada. Explo. Mining Geol., 2, 321-331.

Mei, A., Li, X., Liu, L., Ku, Z., Liu, T., Rong, Y., Xu, M., Hu, M., Chen, J., Yang, Y. and Grätzel, M. (2014) A hole-conductor–free, fully printable mesoscopic perovskite solar cell with high stability. Science, 345, 295-298.

Meinhold, G. (2010) Rutile and its applications in earth sciences. Earth-Science Reviews, 102, 1-28.

Mercadier, J., Richard, A., & Cathelineau, M. (2012). Boron-and magnesium-rich marine brines at the origin of giant unconformity-related uranium deposits: δ11B evidence from Mg-tourmalines. Geology, 40(3), 231-234.

Meyer, M., John, T., Brandt, S., and Klemd, R. (2011) Trace element composition of rutile and the application of Zr-in-rutile thermometry to UHT metamorphism (Epupa Complex, NW Namibia). Lithos, 126, 388-401.

Morad, S. (1986) SEM study of authigenic rutile, anatase and brookite in Proterozoic sandstones from Sweden. Sedimentary Geology, 46, 77-89.

Morad, S., and Aldahan, A. L. A. (1986) Alteration of detrital Fe-Ti oxides in sedimentary rocks. Geological Society of America Bulletin, 97, 567-578.

Navrotsky, A. (2003) Energetics of nanoparticle oxides: interplay between surface energy and polymorphism. Geochemical Transactions, 4, 34.

Ng, R., Alexandre, P., and Kyser, K. (2013) Mineralogical and geochemical evolution of the unconformity-related McArthur River Zone 4 orebody in the Athabasca Basin, Canada: implications of a silicified zone. Economic Geology, 108, 1657-1689.

Osborn, E. F. (1953) Subsolidus reactions in oxide systems in the presence of water at high pressures. Journal of the American Ceramic Society, 36, 147-151.

Pe-Piper, G., Karim, A., and Piper, D. J. (2011) Authigenesis of titania minerals and the mobility of Ti: new evidence from pro-deltaic sandstones, Cretaceous Scotian Basin, Canada. Journal of Sedimentary Research, 81, 762-773.

Pereira, I., Storey, C., Darling, J., Lana, C., and Alkmim, A. R. (2019) Two billion years of evolution enclosed in hydrothermal rutile: Recycling of the São Francisco Craton Crust and constraints on gold remobilisation processes. Gondwana Research, 68, 69-92.

Plavsa, D., Reddy, S. M., Agangi, A., Clark, C., Kylander-Clark, A., and Tiddy, C. J. (2018) Microstructural, trace element and geochronological characterization of TiO2 polymorphs and implications for mineral exploration. Chemical Geology, 476, 130-149.

Rabbia, O. M., Hernández, L. B., French, D. H., King, R. W., and Ayers, J. C. (2009) The El Teniente porphyry Cu–Mo deposit from a hydrothermal rutile perspective. Mineralium Deposita, 44, 849.

Ranade, M. R., Navrotsky, A., Zhang, H. Z., Banfield, J. F., Elder, S. H., Zaban, A., ... and Whitfield, H. J. (2002) Energetics of nanocrystalline TiO2. Proceedings of the National Academy of Sciences, 99, 6476-6481.

Reid, K. D., Ansdell, K., Jiricka, D., Witt, G., and Card, C. (2014) Regional setting, geology, and paragenesis of the Centennial unconformity-related uranium deposit, Athabasca Basin, Saskatchewan, Canada. Economic Geology, 109, 539-566.

Rudnick, R. L., and Gao, S. (2003) Composition of the continental crust. Treatise on geochemistry, 3, 659.

Schandl, E. S., Davis, D. W., and Krogh, T. E. (1990) Are the alteration halos of massive sulfide deposits syngenetic? Evidence from U-Pb dating of hydrothermal rutile at the Kidd volcanic center, Abitibi subprovince, Canada. Geology, 18, 505-508.

Schwartz, G. M. (1958) Alteration of biotite under mesothermal conditions. Economic Geology, 53, 164-177.

Scott, K. M. (2005) Rutile geochemistry as a guide to porphyry Cu–Au mineralization, Northparkes, new South Wales, Australia. Geochemistry: Exploration, Environment, Analysis, 5, 247-253.

Scott, K. M., and Radford, N. W. (2007) Rutile compositions at the Big Bell Au deposit as a guide for exploration. Geochemistry: Exploration, Environment, Analysis, 7, 353-361.

Smith, S. J., Stevens, R., Liu, S., Li, G., Navrotsky, A., Boerio-Goates, J., and Woodfield, B. F. (2009) Heat capacities and thermodynamic functions of TiO2 anatase and rutile: Analysis of phase stability. American Mineralogist, 94, 236-243.

Smyth, J. R. (2006) Hydrogen in high pressure silicate and oxide mineral structures. Reviews in Mineralogy and Geochemistry, 62, 85-115.

Soffer, B. H. (1961) Studies of the optical and infrared absorption spectra of rutile single crystals. The Journal of Chemical Physics, 35, 940-945.

Stepanov, A. S., and Hermann, J. (2013) Fractionation of Nb and Ta by biotite and phengite: Implications for the “missing Nb paradox”. Geology, 41, 303-306.

Swope, R. J., Smyth, J. R., and Larson, A. C. (1995) H in rutile-type compounds: I. Single-crystal neutron and X-ray diffraction study of H in rutile. American Mineralogist, 80, 448-453.

Triebold, S., Luvizotto, G. L., Tolosana-Delgado, R., Zack, T., and von Eynatten, H. (2011) Discrimination of TiO_2 polymorphs in sedimentary and metamorphic rocks. Contributions to Mineralogy and Petrology, 161(4), 581-596.

Tompsett, G. A., Bowmaker, G. A., Cooney, R. P., Metson, J. B., Rodgers, K. A., and Seakins, J. M. (1995) The Raman spectrum of brookite, TiO2 (PBCA, Z= 8). Journal of Raman Spectroscopy, 26, 57-62.

Urban, A. J., Hoskins, B. F., and Grey, I. E. (1992) Characterization of V-Sb-W-bearing rutile from the Hemlo gold deposit, Ontario. The Canadian Mineralogist, 30, 319-326.

Vikre, P.G. and John D.A., 2010 Chapter L. Hydrothermal alteration.in Descriptive Models for Epithermal Gold-Silver Deposits, 125-142.

Vlassopoulos, D., Rossman, G. R., and Haggerty, S. E. (1993) Coupled substitution of H and minor elements in rutile and the implications of high OH contents in Nb-and Cr-rich rutile from the upper mantle. American Mineralogist, 78, 1181-1191.

Wright, D.M., Potter, E.G., and Comeau, J-S., (2015) Athabasca Basin Uranium Geochemistry Database v.2; Geological Survey of Canada, Open File 7792, 1 .zip file. doi:10.4095/296461

Zack, T., and Kooijman, E. (2017) Petrology and geochronology of rutile. Reviews in Mineralogy and Geochemistry, 83, 443-467.

Zeh, A., Cabral, A. R., Koglin, N., and Decker, M. (2018) Rutile alteration and authigenic growth in metasandstones of the Moeda Formation, Minas Gerais, Brazil–A result of Transamazonian fluid–rock interaction. Chemical Geology, 483, 397-409.

Zhang, H., and Banfield, J. F. (1999) New kinetic model for the nanocrystalline anatase-to-rutile transformation revealing rate dependence on number of particles. American Mineralogist, 84, 528-535.

Zhang, H., and Banfield, J. F. (2000) Understanding polymorphic phase transformation behavior during growth of nanocrystalline aggregates: insights from TiO2. The Journal of Physical Chemistry B, 104, 3481-3487.

List of Figure Captions

Figure 1. a) A simplified sketch of Canada showing the locations of the Athabasca and Thelon Basins, and map b. b) A regional map (modified from Jefferson et al. 2007) showing the stratigraphic units of the eastern Athabasca Basin overlying the Rae and Hearne Provinces. The location of the Wollaston Supergroup, the McArthur River deposit, P2 fault, and map c is also shown. Stratigraphic units: RD = Read Formation, MFb = Bird Member, Manitou Falls Formation, MFc = Collins Member, Manitou Falls Formation, MFd = Dunlop Member, Manitou Falls Formation. c) A plan view map (modified from Adlakha et al. 2017 and updated according to Bray et al. 2018) of the unconformity showing the P2 fault, mineralized zones of the McArthur River deposit (from southwest to northeast: McA South 1, Zones 4-1, McA North 1, Zone A, McA North 2, Zone B, McA North 3, and McA North 4), low-grade (P2 Main) and unmineralized areas. Surface drillhole collar locations are indicated by a circle, and next to each drillhole collar is a list of samples that were collect from that location (see Table 1). Samples collected from drillholes collared in the underground mine are indicated with an arrow pointing to its general location (i.e. mineralized zone)

Figure 2. Photographs of representative samples: a) brecciated graphitic (Gr) metapelite with luecosome, b) brecciated quartzite, c) silicified (Qtz) graphitic metapelite overprinted by desilicification and clay, d) silicificied metapelite cross-cut by blue veinlets of magnesio-foitite (Mgf), e) graphitic metapelite pervasively altered to form magnesio-foitite, f) metapelite cross-cut by pegmatite (right side), g) graphitic metapelite crosscut by a vein of uraninite (pointed with an arrow) surrounded by alteration halo of hematite (Hem), and h) hematized, conglomeratic quartz sandstone exhibiting silty layers that contain Ti-oxide. Scale bars = 1 cm

Figure 3. Representative Raman spectra for a) rutile and b) anatase.

Figure 4. Paragenetic sequence of rutile, anatase and co-existing phases, along the P2 fault, with respect to the development of the Athabasca Basin. Dashed lines indicate uncertainty. OG = quartz overgrowths; remob. = remobilized or secondary U-hydroxide

Figure 5. Photomicrographs (transmitted and reflected light) and SEM-BSE images of rutile. a) Disseminated rutile (Type 1) with oxy-dravite (Dv) overprinted by magnesio-foitite with fine-grained anatase (Ant). b) Rutile (Type 1) interlocked with anhedral oxy-dravite and surrounded by lathlike graphite (Gr) and subhedral pyrite (Py). Graphite embays a chloritized mineral interpreted to have been cordierite (Crd). c) Rutile (Type 1) with muscovite (Ms), zircon, graphite, oxy-dravite, and quartz, overprinted by magnesio-foitite. Rutile needles (Type 3) along the muscovite cleavage planes. d) Fractured rutile (Type 1) surrounded by fine-grained uranium oxide (U), sudoite (Sud), and illite (Ilt). e) Rutile (Type 1) with muscovite and quartz containing sillimanite (Sil) needles. An inset BSE image shows muscovite (Ms) with rutile and zircon. Reddish color of muscovite is due to alteration forming fine-grained Fe-oxide. f) Fine-grained blocky rutile (Type 2) with rounded inclusions of anatase (Ant^{r}) in an unknown coarse-grained mineral (?) that is surrounded by sudoite and stringers of hematite (Hem). Sudoite with patchy, and dendritic anatase (Ant^{p}, Ant^{d}, respectively) alter the mineral.

Figure 6. Photomicrographs (transmitted and reflected light) and SEM-BSE images of anatase. a) Anatase (Ant) with dolomite (Dol) and coarse-grained hematite (Hem). An inset BSE image showing zoned anatase with a core containing high W and Fe. b) A silty layer containing anatase in quartz (Qz) sandstone. An inset BSE image showing anatase with late diagenetic illite (Ilt). c) Anatase overprinting kaolin (Kln) and quartz overgrowths of detrital quartz. Quartz overgrowths

containing Sr-SO_4 rich APS minerals. Note black triangular grains (bottom right) are diamond grit from polish paste trapped in clay. d) Lath-like anatase partially replaced by U-oxide. e) Anatase with magnesio-foitite surrounding early rutile (Rt) and zircon (Zr). f) Coarse-grained disseminated anatase.

Figure 7. Biplots of element abundances in rutile using EPMA data recalculated as atomic cation percent: a) Ti and V, b) Nb and V, c) Nb and Fe, and d) Nb and V+Fe. Trendlines rooted at zero are shown representing different substitution mechanisms.

Figure 8. Biplots of element abundances in anatase using EPMA data recalculated as atomic cation percent: a) Ti and V, b) Nb and Fe, c) W and Fe, and d) Ti and Fe. Trendlines rooted at zero are shown representing different substitution mechanisms.

Figure 9. Biplot diagrams showing LA-ICP-MS data for rutile and anatase: a) Ta vs. Nb/Ta, b) Zr/Hf vs. Nb/Ta, and c) Th vs. U (in ppm), d) Fe/Nb vs V/Fe. The grey and orange fields in a and b are for rutile in high-grade metasedimentary rocks from Luvizotto and Zack (2009) and Meyer et al (2011), respectively. Lower Zr/Hf ratios reported by Meyer et al. (2011) shown in b are explained by recrystallization by fluids during retrogression. The hydrothermal and mantle fields shown in diagram b are modified from Pereira et al. (2019). Triangle markers indicate rutile that occurs with oxy-dravite. Open diamonds represent anatase hosted in sandstone samples, whereas filled diamonds represent anatase in basement metapelite. Color coding reflects sample position along the P2 fault: green for unmineralized areas, blue for low-grade mineralized areas, purple for Zone 1, red for Zone 2 and orange for Zone 4 (see Fig. 1C).

Tables

Table 1. Sample list and descriptions

DDH[a]	Sample	Depth (m)[b]	Lithology[c]	U mineralization[d]	Ti species[e]	Size (µm)	Crystal habit
MC349	MAC98	578	metapelite breccia/ gouge	low grade	Rt	20 - 100	Subhedral, fractured with corroded rims
					Ant	10 - 50	Blocky to dendritic fracture infill, rare euhedral crystal observed
MC349	MAC99	573	quartz+oxy-dravite graphitic metapelite breccia with intense magnesio-foitite alteration	low grade	Rt	50 - 150	Subhedral, fractured crystals
H3559	MAC201	-	quartz+oxy-dravite vein in graphitic metapelite	Z1	Rt	50 - 500	Subhedral to rounded, clean to corroded rims
H3576	MAC203	-	metapelite with luecosome	Z1	Rt	200 - 400	Subhedral, heavily fractured with corroded rims
H203	MAC152	-	graphitic metapelite	Z2	Rt	100 - 400	Subhedral, fractured with corroded rims
H203	MAC444	-	graphitic metapelite with 1 cm wide leucosome	Z2	Rt	50 - 300	Subhedral, fractured with corroded rims
H201	MAC70	-	graphitic metapelite breccia	Z2	Rt	20 - 100	Subhedral, fractured with corroded rims
H201	MAC441	-	graphitic metapelite with leucosome patches	Z2	Rt	50 - 200	Subhedral, fractured with corroded rims
H347	MAC79		yellow-clay altered quartzite breccia	Z2	Rt	50 – 500	Sub-anhedral, fractured
H493	MAC84	-	quartz+oxy-dravite graphitic metapelite breccia	Z2	Rt	50 - 200	Subhedral, fractured with corroded rims
H493	MAC86	-	graphitic metapelite with luecosomes breccia	Z2	Rt	50 - 150	Subhedral, fractured with corroded rims
H3380	MAC423	-	uraninite-hematite vein in graphitic metapelite	Z2	Ant	< 50	Blocky clusters to lath-like, coated in U oxide
H677	MAC420	-	metapelite with l0 cm wide pegmatite	Z4	Rt	50 - 400	Subhedral, fractured with corroded rims
MC410	MAC406	527.7	hematized, conglomeratic quartz sandstone	low grade	Ant	20 - 100	Blocky to anhedral patches
MC362	MAC127	602.3	graphitic metapelite breccia with luecosomes	unmin	Rt	40 - 250	Subhedral, fractured crystals
MC359	MAC426	581.6	local hematite-dolomite in graphitic metapelite	unmin	Ant	< 100	Euhedral to anhedral crystals with corroded rims
MC359	MAC430	494	hematized, conglomeratic quartz sandstone	unmin	Ant	< 50	Blocky to anhedral clusters
MC381	MAC436	603	quartz+oxy-dravite graphitic metapelite breccia with intense magnesio-foitite alteration	unmin	Rt	20 - 100	Euhedral crystals with corroded rims
					Ant	< 10	Blocky disseminations

a: diamond drill-hole; b: depth from surface; b: - = collared underground; c: pel = metapelite, peg = pegmatite, ss = sandstone, gr = graphitic, bx = breccia; d: unmin = no mineralization, low grade = sub-economic area, Z1-4 = Zone # ore body of the McArthur River deposit; e: Rt = Rutile, Ant = anatase

Table 2. Types of Ti-oxide occurrences

Mineral	Type	Mode of Occurrence	Spatially Associated minerals	Samples
Rutile[a]				
	Type 1	disseminated	oxy-dravite, graphite, pyrite, quartz, zircon	MAC84, MAC99, MAC127, MAC201, MAC420 MAC436
			quartz, graphite, pyrite, zircon,	MAC70, MAC86, MAC441, MAC444
			quartz	MAC98, MAC152, MAC203
			quartz, sillimanite, zircon, Fe-oxide altered muscovite	MAC79 (quartzite)
	Type 2	fg needles along cleavages of mica	chloritized muscovite	MAC70, MAC84, MAC86, MAC127, MAC423, MAC441, MAC444
	Type 3	fg blocky inclusions	altered amphibole, rounded anatase	MAC98
Anatase				
	SS-hosted	anhedral, patchy grains interstitial to detrital minerals	illite, kaolin, APS minerals, fg red hematite	MAC406, MAC430
	Basement-hosted	fg to cg anhedral disseminations	magnesio-foitite, sudoite, illite, LREE-rich APS minerals, late U-oxide	MAC98, MAC436
		lath-like mica pseudomorphs	U-oxide, magnesio-foitite, sudoite, illite, LREE-rich APS minerals, late U-oxide	MAC423
		rounded inclusions	Type 2 rutile	MAC98
		dendritic veinlets and anhedral patchy grains	Sudoite, fg red hematite, LREE-rich APS, late U-oxide	MAC98
		euhedral cg crystals	dolomite, cg black hematite	MAC426

cg = coarse-grained, fg = fine-grained; Notes: a: All rutile occurs in basement rocks.

Table 3. Average composition of rutile in wt.% (EPMA) and ppm (LA-ICP-MS) with standard deviation (1σ)

Sample	MAC152		MAC201		MAC70		MAC86		MAC420	
wt.%; n =	48/11		33/9		19/8		14/6		18/9	
	x̄	±	x̄	±	x̄	±	x̄	±	x̄	±
Cr	0.15	0.10	0.03	0.01	0.13	0.02	0.11	0.04	0.13	0.03
Nb	0.32	0.05	0.33	0.09	0.33	0.10	0.29	0.09	0.30	0.13
Zr	0.07	0.02	0.08	0.03	0.06	0.02	0.06	0.02	0.07	0.03
Ta	<0.01		<0.01		<0.01		<0.01		<0.01	
Ti	59.32	0.19	59.51	0.22	59.46	0.25	59.32	0.17	59.53	0.27
W	0.08	0.03	0.21	0.05	0.05	0.03	0.06	0.03	0.07	0.05
V	0.23	0.12	0.28	0.03	0.30	0.03	0.58	0.13	0.30	0.10
Fe	0.11	0.04	0.16	0.03	0.07	0.03	0.05	0.02	0.08	0.04
O	40.07	0.09	40.22	0.11	40.19	0.14	40.19	0.1	40.21	0.06
Total	100.41	0.20	100.86	0.26	100.66	0.39	100.75	0.25	100.75	0.14
ppm; n =	12/9		14/11		6/6		9/8		10/10	
Al	264	128	183	76.8	1780	2380	720	933	1740	4490
Si	205	391	114	210	3610	3847	763	957	4980	6910
Ca	3.17	7.09	25.9	27.5	44.7	31.9	12.6	19.6	23.4	33.4
Sc	211	126.0	102	5.68	93.2	9.29	73.2	8.03	93.9	19.0
V	3540	1210	3890	222	4610	777	6620	1520	4360	873
Cr	1660	837	407	39.1	1560	344	1090	304	1390	228
Mn	1.66	1.52	0.64	0.86	3.35	1.75	1.51	1.50	1.47	1.53
Fe	830	370	1410	240	837	445	437	220	883	454
Co	0.110	0.144	0.008	0.013	0.657	0.824	0.176	0.273	13.2	29.7
Ni	0.236	0.351	0.371	0.160	1.44	1.61	1.01	1.10	11.5	29.0
Cu	3.47	2.81	1.50	0.354	4.81	4.10	1.53	0.29	1.15	0.572
Zn	4.59	1.56	6.79	1.50	6.13	2.79	4.99	1.40	3.69	0.63
Ga	0.482	0.184	0.696	0.586	1.29	1.50	0.536	0.460	1.07	2.16
Ge	1.76	1.03	0.729	0.683	0.333	0.553	0.833	0.512	1.03	0.934
Se	14.7	23.5	36.9	50.7	14.5	15.9	14.4	30.1	5.00	15.0
Y	0.312	0.518	0.077	0.092	1.47	1.69	0.387	0.280	0.391	0.610
Zr	743	136	867	140	656	126	616	96.9	726	207
Nb	2970	302	3080	615	3060	939	3010	442	3460	1060
Mo	7.91	3.39	7.05	3.22	6.51	5.67	9.42	6.55	9.43	3.94
Sn	212	31.8	93.1	12.7	188	13.1	206	11.3	219	21.3
Sb	1.17	0.544	0.246	0.303	1.34	0.447	1.41	0.263	1.01	0.325
Hf	45.5	6.12	47.5	6.12	36.9	4.84	35.1	3.15	42.2	13.3
Ta	290	65.2	230	60.4	176	48.9	177	86.6	330	133
W	963	76.2	2540	295	684	207	852	103	992	450
Pb	0.257	0.467	0.070	0.053	2.47	2.82	0.836	0.782	0.262	0.277
Th	0.742	1.47	0.237	0.426	10.7	15.6	3.37	2.63	3.68	6.01
U	69.6	10.4	30.7	7.72	36.5	6.20	75.0	10.4	39.0	7.08

Note: EPMA data of Al, Si, Th, U, Mn, Mo were close to or below detection limits. Numbers below sample numbers indicate: number of data points/ number of grains. All data is of Type 1 disseminated rutile, except for MAC98T3 which is of Type 3 rutile inclusions.

Table 3. continued

Sample	MAC441		MAC84		MAC127		MAC203		MAC79	
wt.%; n =	21/6		27/10		27/12		(6/2)		8/4	
	x̄	±	x̄	±	x̄	±	x̄	±	x̄	±
Cr	0.12	0.02	0.07	0.03	0.13	0.03	0.03	0.03	0.13	0.02
Nb	0.41	0.10	0.26	0.02	0.22	0.12	0.69	0.11	0.92	0.11
Zr	0.08	0.02	0.07	0.02	0.07	0.02	0.12	0.02	0.08	0.03
Ta	<0.01		<0.01		<0.01		0.05	0.02	0.06	0.07
Ti	59.34	0.57	58.77	0.32	59.39	0.25	59.00	0.20	58.69	0.22
W	0.04	0.02	0.39	0.04	0.02	0.02	0.17	0.04	0.08	0.02
V	0.18	0.02	0.99	0.23	0.58	0.11	0.10	0.05	0.10	0.05
Fe	0.15	0.04	0.05	0.02	0.06	0.02	0.30	0.07	0.38	0.07
O	40.16	0.25	40.03	0.13	40.18	0.12	40.05	0.09	39.99	0.11
Total	100.59	0.63	100.67	0.29	100.70	0.30	100.55	0.20	100.48	0.28
ppm; n =	10/10		8/7		10/9		9/6		6/5	
Al	264	136	81.3	76.1	106	61	497	141	265	83
Si	124	249	66.3	175	219	318	382	419	3270	5450
Ca	38.0	40.0	16.0	27.8	26.8	32.7	13.3	18.0	8.33	18.6
Sc	94.1	13.0	97.2	27.0	92.9	15.4	774	185	94.9	4.10
V	2650	306	12100	2540	6370	1240	1840	362	2170	333
Cr	1260	209	904	277	1220	105	258	127	1210	206
Mn	0.66	1.17	2.63	6.91	0.88	0.82	1.87	1.13	0.87	0.90
Fe	1560	480	197	129	410	53	2780	580	3270	954
Co	0.001	0.004	0.029	0.048	0.008	0.010	0.001	0.004	0.026	0.027
Ni	0.098	0.126	0.115	0.115	0.216	0.166	0.086	0.169	0.032	0.038
Cu	0.791	0.229	1.50	0.554	0.956	0.259	0.894	0.143	1.84	0.755
Zn	3.03	1.67	4.94	1.07	3.35	1.38	3.26	0.92	5.83	2.67
Ga	0.920	0.655	0.175	0.226	0.465	0.425	2.84	0.595	0.815	0.277
Ge	0.650	0.879	1.41	1.06	0.960	0.880	0.489	0.614	0.433	0.556
Se	25.5	22.9	2.00	5.29	6.70	11.1	16.2	15.4	15.8	16.5
Y	0.026	0.006	0.166	0.248	1.65	4.84	0.106	0.161	3.58	7.79
Zr	816	75.9	623	63.5	699	91.1	1010	53.2	638	130
Nb	5410	2660	2580	248	2060	606	7770	1140	7860	1870
Mo	3.84	0.725	5.45	4.86	10.7	7.13	14.1	4.00	19.1	11.5
Sn	162	13.1	389	27.1	181	8.89	238	80.0	204	17.2
Sb	0.305	0.229	0.765	0.353	1.15	0.258	0.573	0.328	0.433	0.253
Hf	43.7	3.56	36.8	3.12	35.5	3.37	52.5	2.57	33.3	7.31
Ta	458	297	225	36.7	147	90.9	711	173	721	321
W	514	118	4440	226	219	34.0	1920	422	1040	229
Pb	0.023	0.026	0.299	0.466	0.594	1.68	0.031	0.059	0.262	0.487
Th	0.00	0.00	1.72	3.02	2.34	7.02	0.148	0.418	0.517	1.15
U	16.5	1.22	92.7	9.67	77.5	16.5	23.5	1.79	51.2	9.30

Table 3. continued

Sample	MAC99		MAC444		MAC436		MAC98		MAC98-T2	
wt.%; n =	18/10		12/5		12/7		13/5		5/5	
	x̄	±	x̄	±	x̄	±	x̄	±	x̄	±
Cr	0.02	0.01	0.18	0.03	0.10	0.02	0.12	0.05	0.14	0.02
Nb	0.77	0.08	0.25	0.07	0.24	0.05	2.33	0.39	2.23	0.15
Zr	0.07	0.01	0.07	0.02	0.07	0.02	0.07	0.02	0.02	0.02
Ta	<0.01		<0.01		<0.01		0.14	0.11	0.02	0.03
Ti	59.04	0.17	59.18	0.16	59.21	0.24	56.54	0.70	56.59	0.61
W	0.05	0.03	0.06	0.03	0.18	0.03	0.35	0.15	0.07	0.05
V	0.13	0.02	0.64	0.15	0.49	0.06	0.84	0.12	1.10	0.10
Fe	0.37	0.07	0.04	0.02	0.04	0.01	0.61	0.17	0.33	0.21
O	40.1	0.09	40.1	0.03	40.06	0.17	39.71	0.14	39.65	0.27
Total	100.60	0.22	100.56	0.11	100.46	0.46	100.84	0.21	100.32	0.68
ppm; n =	10/8		9/9		10/10		3/3			
Al	327	119	76.8	150	80.9	34.8	628	173		
Si	350	346	602	1039	168	339	877	996		
Ca	19.1	31.3	29.9	32.6	5.7	8.61	12.3	10.2		
Sc	90.8	9.04	95.4	18.2	94.8	16.5	142	17.6		
V	2280	193	6820	1330	5760	1090	10200	996		
Cr	322	26.1	1490	465	1110	232	1370	367		
Mn	0.97	1.55	1.52	1.71	0.42	0.77	1.57	1.14		
Fe	2980	521	235	78.2	352	158	6010	997		
Co	0.008	0.023	0.035	0.048	0.008	0.012	0.015	0.015		
Ni	0.124	0.187	0.187	0.197	0.220	0.166	0.337	0.104		
Cu	1.31	0.164	0.898	0.207	1.19	0.231	1.31	0.141		
Zn	4.84	1.17	3.31	1.27	3.89	0.98	4.83	1.32		
Ga	1.10	0.389	0.084	0.143	0.335	0.425	2.22	0.684		
Ge	0.980	0.812	0.622	0.739	1.01	0.692	0.967	0.544		
Se	20.7	25.8	7.89	11.6	19.0	24.3	19.0	13.7		
Y	0.057	0.028	0.054	0.074	0.482	1.34	0.057	0.016		
Zr	679	51.7	718	130	719	87.0	621	149		
Nb	7080	1530	2640	497	3140	1180	24200	721		
Mo	5.22	2.87	3.59	2.79	0.771	0.654	11.2	6.60		
Sn	58.5	5.10	147	12.8	215	35.1	297	14.0		
Sb	0.129	0.132	0.579	0.358	0.608	0.271	0.180	0.083		
Hf	37.6	2.87	36.6	5.83	37.8	4.83	35.2	6.16		
Ta	531	142	365	149	349	183	2710	251		
W	633	59.8	495	190	1490	402	4290	907		
Pb	0.070	0.127	0.021	0.025	0.055	0.065	0.020	0.029		
Th	0.033	0.096	0.039	0.110	0.123	0.369	0.000	0.000		
U	10.9	0.747	29.2	9.41	41.0	10.4	24.7	3.82		

Table 4. Averaged composition of anatase in elemental wt.% (EPMA) and ppm (LA-ICP-MS) with standard deviation (1σ).

Sample	MAC426		MAC436		MAC98-inc		MAC98-patchy		MAC430		MAC406	
wt.%; n =	11/6		3/2		(2/1)		(8/6)		11/6		11/8	
	x̄	±	x̄	±	x̄	±	x̄	±	x̄	±	x̄	±
Cr	0.05	0.06	<0.01		<0.01		<0.02		<0.01		<0.01	
Nb	0.18	0.02	0.10	0.07	0.11	0.02	0.06	0.04	0.25	0.10	0.23	0.02
Zr	0.19	0.09	<0.02		0.02	0.01	<0.01		0.06	0.04	0.02	0.02
Ti	59.48	0.77	60.03	0.30	60.13	0.11	59.98	0.15	59.40	0.30	59.45	0.28
W	0.28	0.54	0.02	0.02	<0.01		<0.01		<0.01		<0.01	
V	<0.01		<0.01		<0.01		0.11	0.12	<0.01		<0.01	
Fe	0.31	0.24	0.08	0.01	0.21	0.03	0.18	0.13	0.42	0.15	0.40	0.16
O	40.12	0.27	40.26	0.17	40.35	0.05	40.29	0.08	40.05	0.08	40.09	0.11
Total	100.62	0.32	100.57	0.48	100.78	0.16	100.78	0.16	100.27	0.15	100.32	0.24
ppm; n =	7/7		1/1				1/1		3/3		5/5	
Al	282	608	5850				500		3020	3470	3610	2530
Si	1430	2170	4780				0		17600	12500	4610	3240
Ca	1770	3310	2.00				26		168	80.2	225	62.1
Sc	30.3	21.4	2.29				42.6		101	58.3	64.8	9.62
V	85.5	55.8	12.9				116.9		86.5	50.1	77.8	11.3
Cr	401	287	2.00				259		20.3	9.81	192	22.6
Mn	15.4	28.3	0.000				0.6		5.90	4.34	7.36	1.63
Fe	1480	318	505				1562		4950	1610	5970	941
Co	0.266	0.568	0.035				0		0.016	0.005	0.011	0.012
Ni	0.627	1.33	1.97				0.37		0.073	0.104	0.306	0.169
Cu	1.04	0.405	1.58				1.89		1.06	0.269	2.342	0.442
Zn	3.93	0.928	3.40				4.7		5.67	1.87	4.92	1.21
Ga	0.082	0.183	1.72				0.22		0.977	0.803	1.50	0.606
Ge	0.614	0.541	2.00				1.6		0.467	0.525	0.260	0.520
Se	9.29	15.2	0.000				0		31.7	44.8	18.8	23.0
Y	0.742	0.451	0.111				0.112		4.30	3.28	7.81	1.45
Zr	2610	671	11.4				169.9		559	73.8	463	77.8
Nb	1870	70.7	1160				836		4910	4060	2190	175
Mo	0.077	0.114	0.000				3.1		2.07	0.611	6.57	1.59
Sn	95.8	21.2	0.550				0.39		70.4	96.0	3.10	0.541
Sb	0.026	0.127	0.000				0		3.15	1.60	3.77	0.755
Hf	140	15.4	0.760				2.81		22.9	8.80	14.5	3.09
Ta	158	11.7	35.2				58.7		470	517	119	48.2
W	585	337	51.9				93.8		93.0	36.8	27.0	1.82
Pb	4.02	2.76	0.210				0.82		12.9	8.01	27.2	4.04
Th	30.5	22.2	0.380				3.61		12.0	9.82	37.0	7.25
U	9.74	7.37	1.49				115		71.7	44.8	149	32.0

Note: EPMA of Al, Si, Mg, Mn, Mo, Sn, Ta, Th, U <0.02 wt.%
Number in parentheses below sample numbers indicate: (number of data points/ number of grains) analysed. MAC98inc = rounded inclusions; MAC98-patchy = patchy replacement

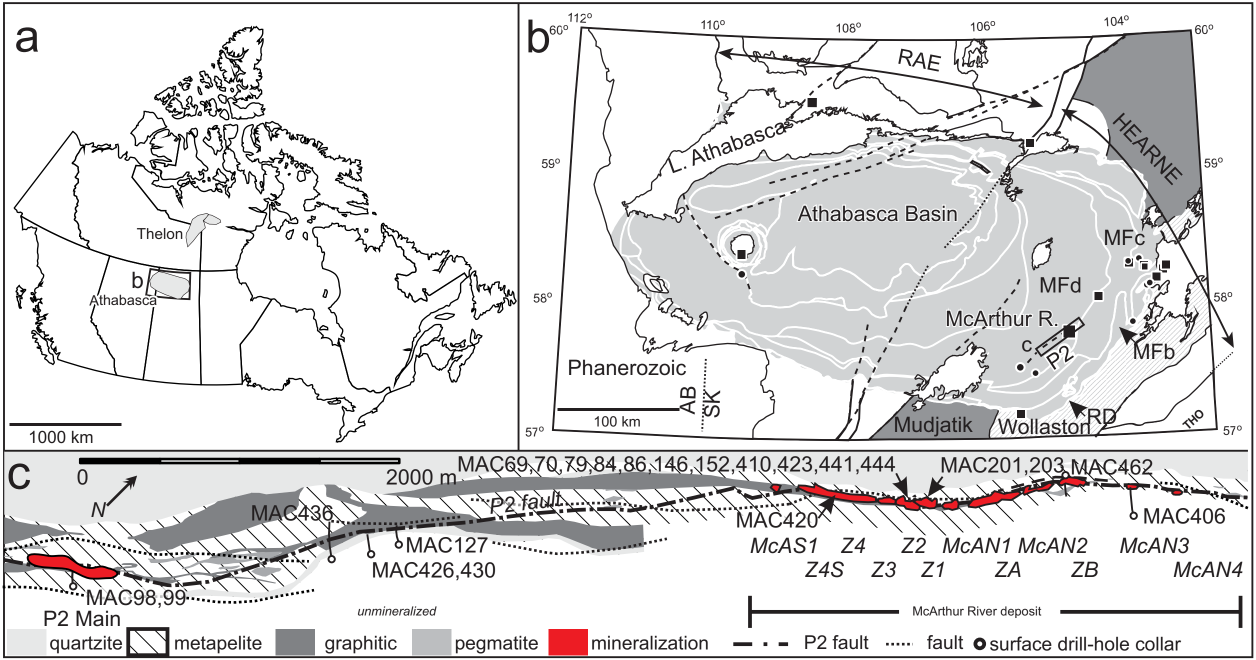
a
Thelon
b
Athabasca
1000 km
b
112°
110°
108°
106°
104°
60°
60°
59°
59°
58°
58°
57°
57°
RAE
HEARNE
L. Athabasca
Athabasca Basin
MFc
MFd
McArthur R.
c
P2
MFb
Phanerozoic
AB
SK
100 km
Mudjatik
Wollaston
RD
THO
c
0
2000 m
N
MAC69,70,79,84,86,146,152,410,423,441,444
MAC201,203
MAC462
P2 fault
MAC436
MAC420
MAC406
MAC127
MAC426,430
MAC98,99
P2 Main
McAS1
Z4
Z2
McAN1
McAN2
McAN3
Z4S
Z3
Z1
ZA
ZB
McAN4
unmineralized
McArthur River deposit
quartzite
metapelite
graphitic
pegmatite
mineralization
P2 fault
fault
surface drill-hole collar

Figure 1

a MAC86 graphitic metapelite breccia
Gr
b MAC79 quartzite breccia
MAC79
c MAC152 graphitic metapelite
Qtz
MAC152
d MAC99 graphitic metapelite breccia
Mgf
MAC 99
e MAC436 graphitic metapelite breccia
Mgf
MAC 436
f MAC420 pegmatite in metapelite
MAC420
g MAC423 U-vein in graphitic metapelite
U
3380 @ 52.6m
h MAC406 conglomeratic quartz sandstone
silty layers
MAC406

Figure 2

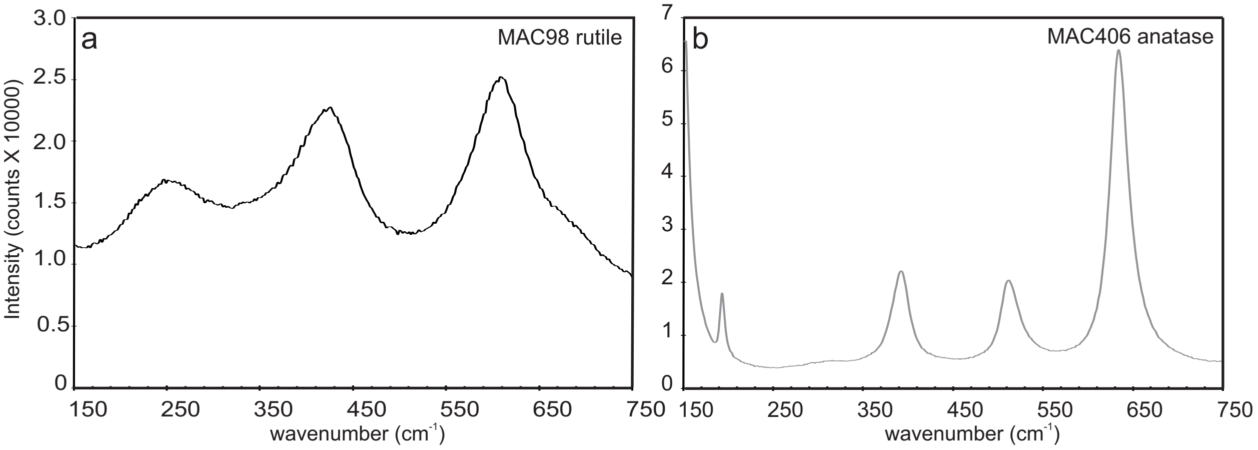

a
MAC98 rutile
Intensity (counts X 10000)
3.0
2.5
2.0
1.5
1.0
0.5
0
150
250
350
450
550
650
750
wavenumber (cm^{-1})
b
MAC406 anatase
7
6
5
4
3
2
1
0
150
250
350
450
550
650
750
wavenumber (cm^{-1})

Figure 3

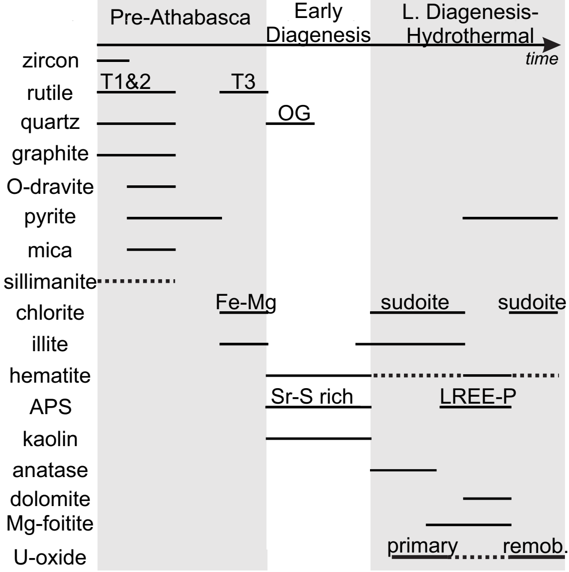
Pre-Athabasca
Early Diagenesis
L. Diagenesis-Hydrothermal
time
zircon
rutile
quartz
graphite
O-dravite
pyrite
mica
sillimanite
chlorite
illite
hematite
APS
kaolin
anatase
dolomite
Mg-foitite
U-oxide
T1&2
T3
OG
Fe-Mg
sudoite
sudoite
Sr-S rich
LREE-P
primary
remob.

Figure 4

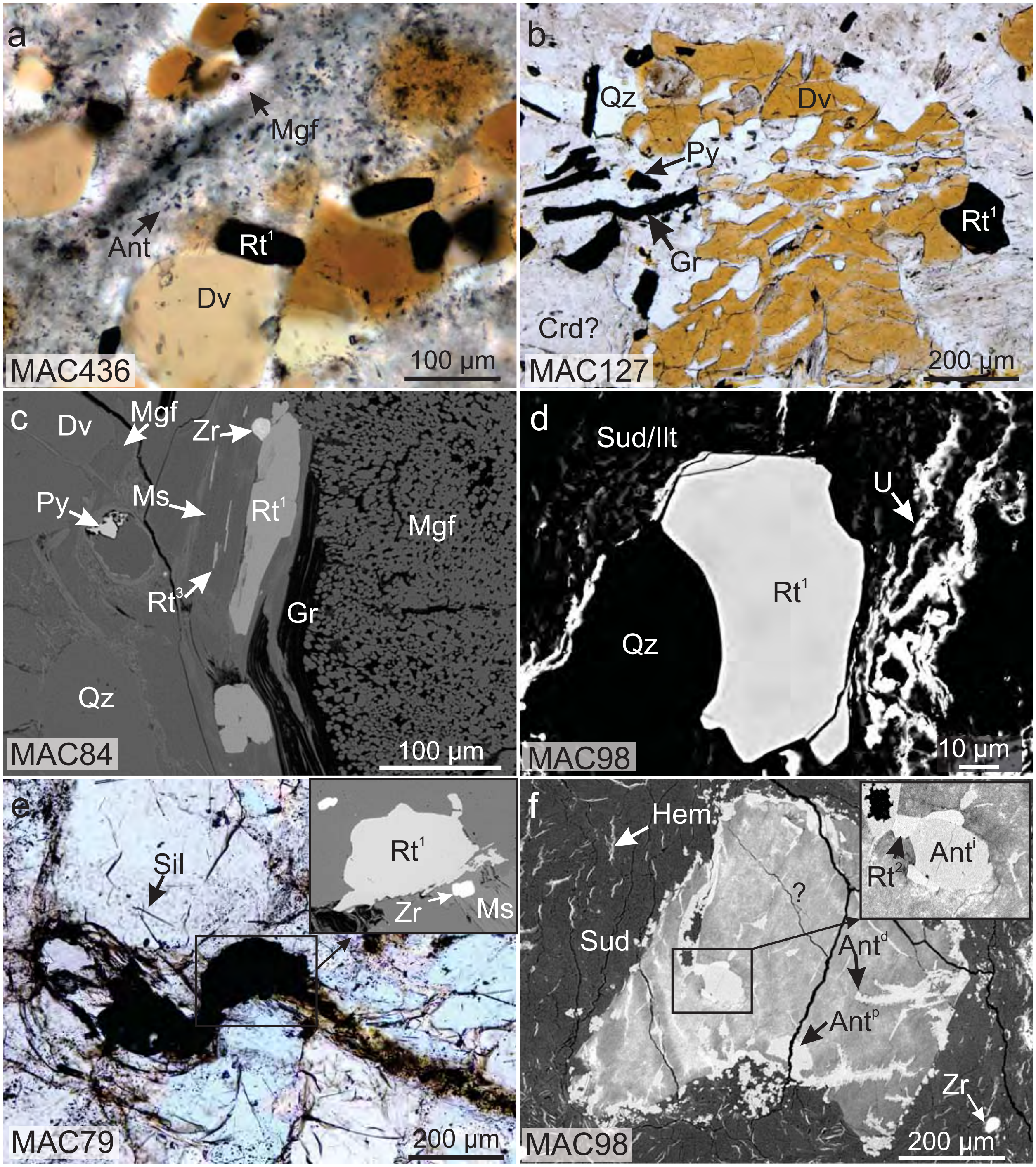
a
Mgf
Ant
Rt^1
Dv
MAC436
100 µm
b
Qz
Dv
Py
Gr
Rt^1
Crd?
MAC127
200 µm
c
Dv
Mgf
Zr
Py
Ms
Rt^1
Mgf
Rt^3
Gr
Qz
MAC84
100 µm
d
Sud/Ilt
U
Rt^1
Qz
MAC98
10 µm
e
Sil
Rt^1
Zr
Ms
MAC79
200 µm
f
Hem
Sud
?
Ant^i
Rt^2
Ant^d
Ant^p
Zr
MAC98
200 µm

Figure 5

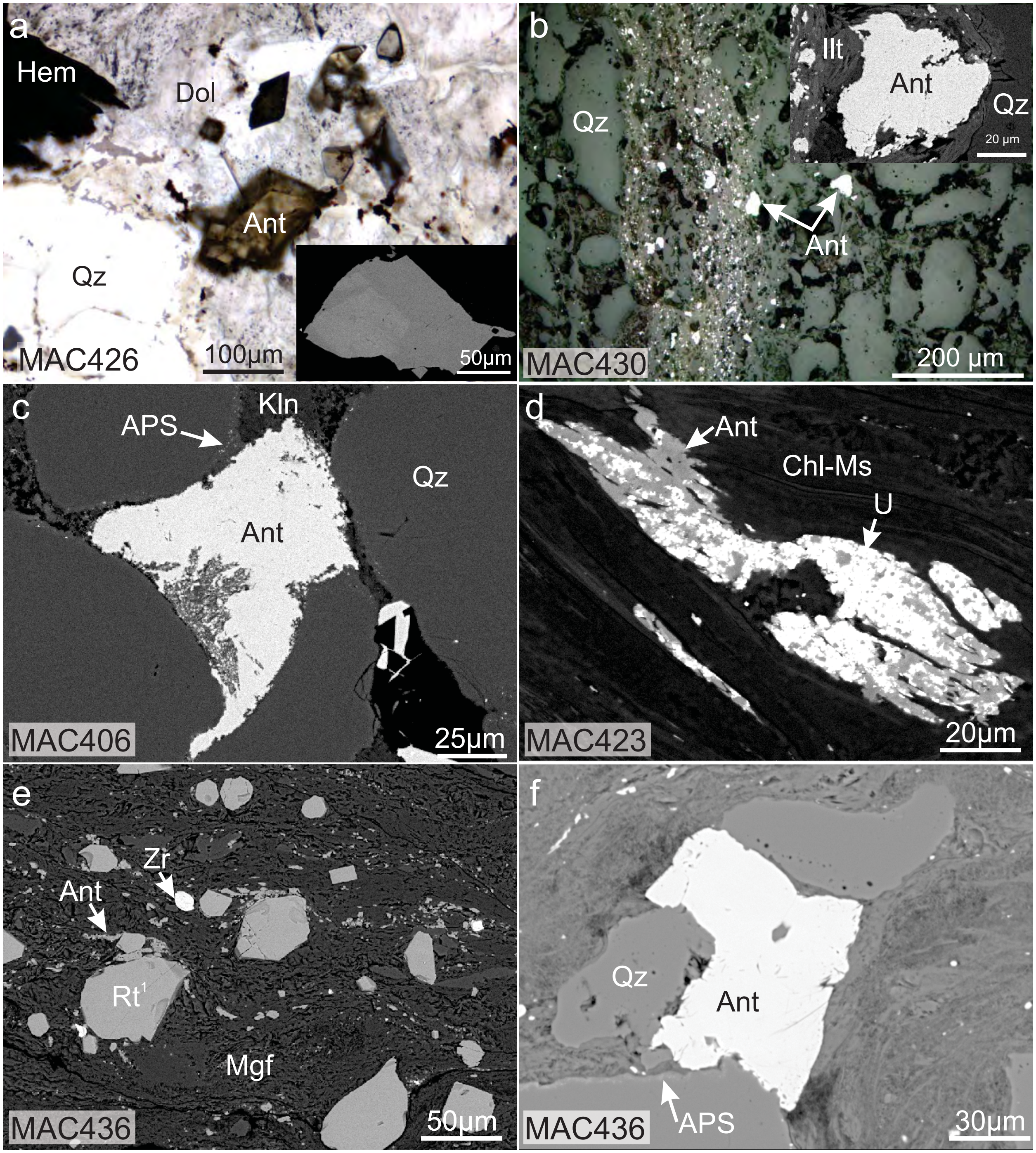
a
Hem
Dol
Ant
Qz
MAC426
100µm
50µm
b
Qz
Ilt
Ant
Qz
20 µm
Ant
MAC430
200 µm
c
APS
Kln
Qz
Ant
MAC406
25µm
d
Ant
Chl-Ms
U
MAC423
20µm
e
Zr
Ant
Rt1
Mgf
MAC436
50µm
f
Qz
Ant
APS
MAC436
30µm

Figure 6

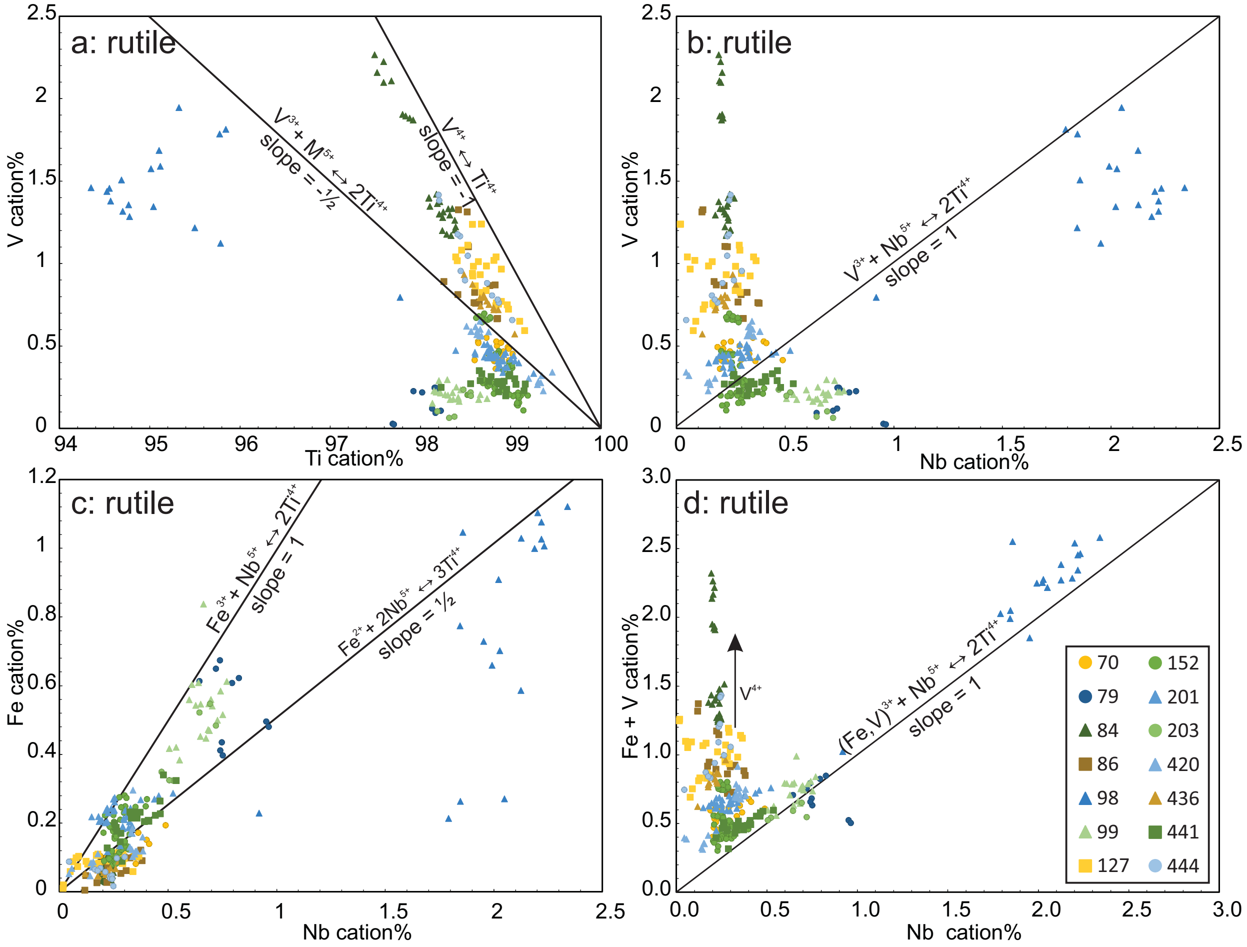
a: rutile
V cation%
Ti cation%
2.5
2
1.5
1
0.5
0
94
95
96
97
98
99
100
V3+ + M5+ ↔ 2Ti4+
slope = -½
V4+ ↔ Ti4+
slope = -1
b: rutile
V cation%
Nb cation%
V3+ + Nb5+ ↔ 2Ti4+
slope = 1
2.5
2
1.5
1
0.5
0
0
0.5
1
1.5
2
2.5
c: rutile
Fe cation%
Nb cation%
1.2
1
0.8
0.6
0.4
0.2
0
0
0.5
1
1.5
2
2.5
Fe3+ + Nb5+ ↔ 2Ti4+
slope = 1
Fe2+ + 2Nb5+ ↔ 3Ti4+
slope = ½
d: rutile
Fe + V cation%
Nb cation%
3.0
2.5
2.0
1.5
1.0
0.5
0.0
0.0
0.5
1.0
1.5
2.0
2.5
3.0
V4+
(Fe,V)3+ + Nb5+ ↔ 2Ti4+
slope = 1
● 70
● 152
● 79
▲ 201
▲ 84
● 203
■ 86
▲ 420
▲ 98
▲ 436
▲ 99
■ 441
■ 127
● 444

Figure 7

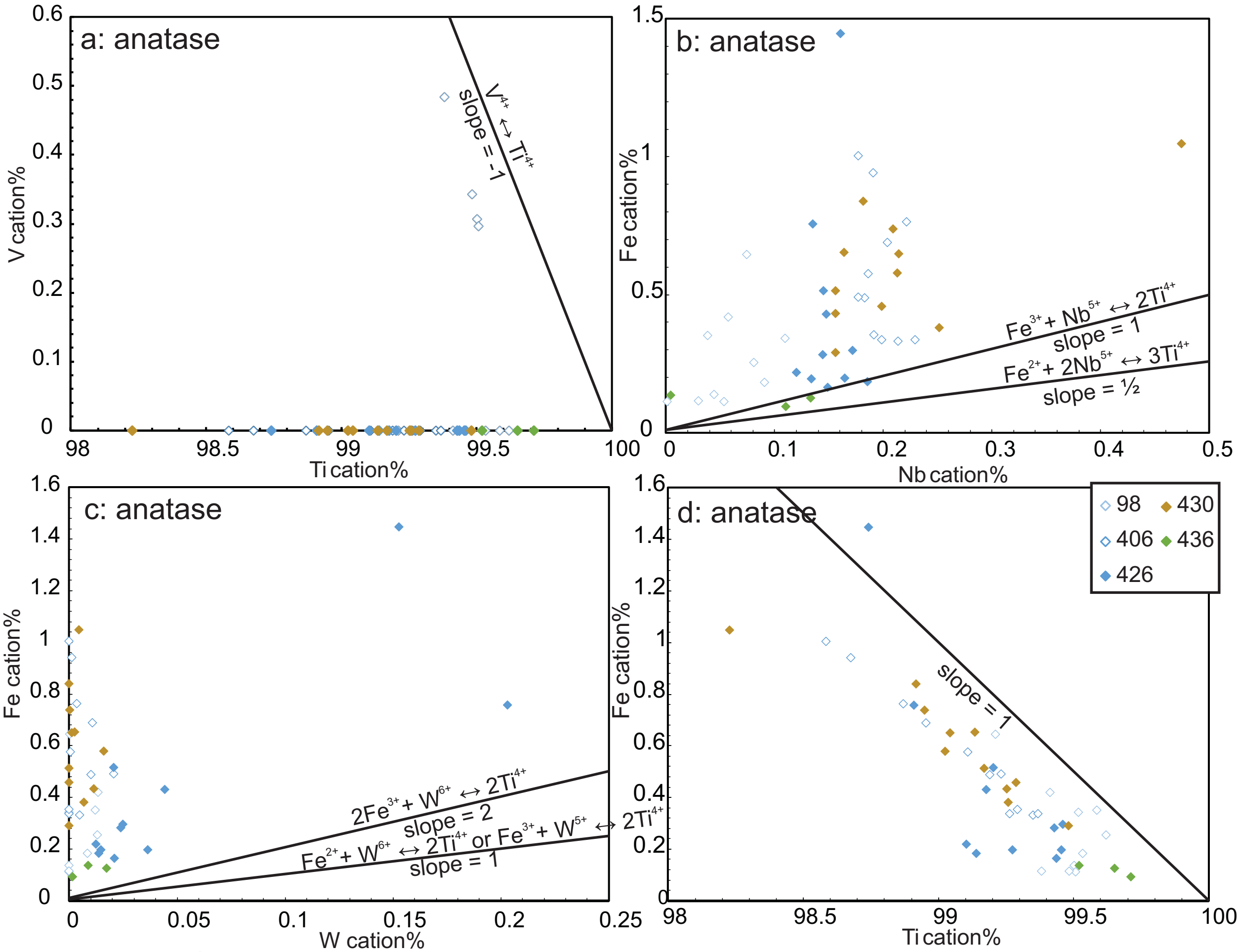
a: anatase
V cation%
Ti cation%
0.6
0.5
0.4
0.3
0.2
0.1
0
98
98.5
99
99.5
100
$V^{4+} \leftrightarrow Ti^{4+}$
slope = -1
b: anatase
Fe cation%
Nb cation%
1.5
1
0.5
0
0.1
0.2
0.3
0.4
0.5
$Fe^{3+} + Nb^{5+} \leftrightarrow 2Ti^{4+}$
slope = 1
$Fe^{2+} + 2Nb^{5+} \leftrightarrow 3Ti^{4+}$
slope = ½
c: anatase
Fe cation%
W cation%
1.6
1.4
1.2
1
0.8
0.6
0.4
0.2
0
0.05
0.1
0.15
0.2
0.25
$2Fe^{3+} + W^{6+} \leftrightarrow 2Ti^{4+}$
slope = 2
$Fe^{2+} + W^{6+} \leftrightarrow 2Ti^{4+}$ or $Fe^{3+} + W^{5+} \leftrightarrow 2Ti^{4+}$
slope = 1
d: anatase
Fe cation%
Ti cation%
slope = 1
◇ 98
◆ 430
◇ 406
◆ 436
◆ 426

Figure 8

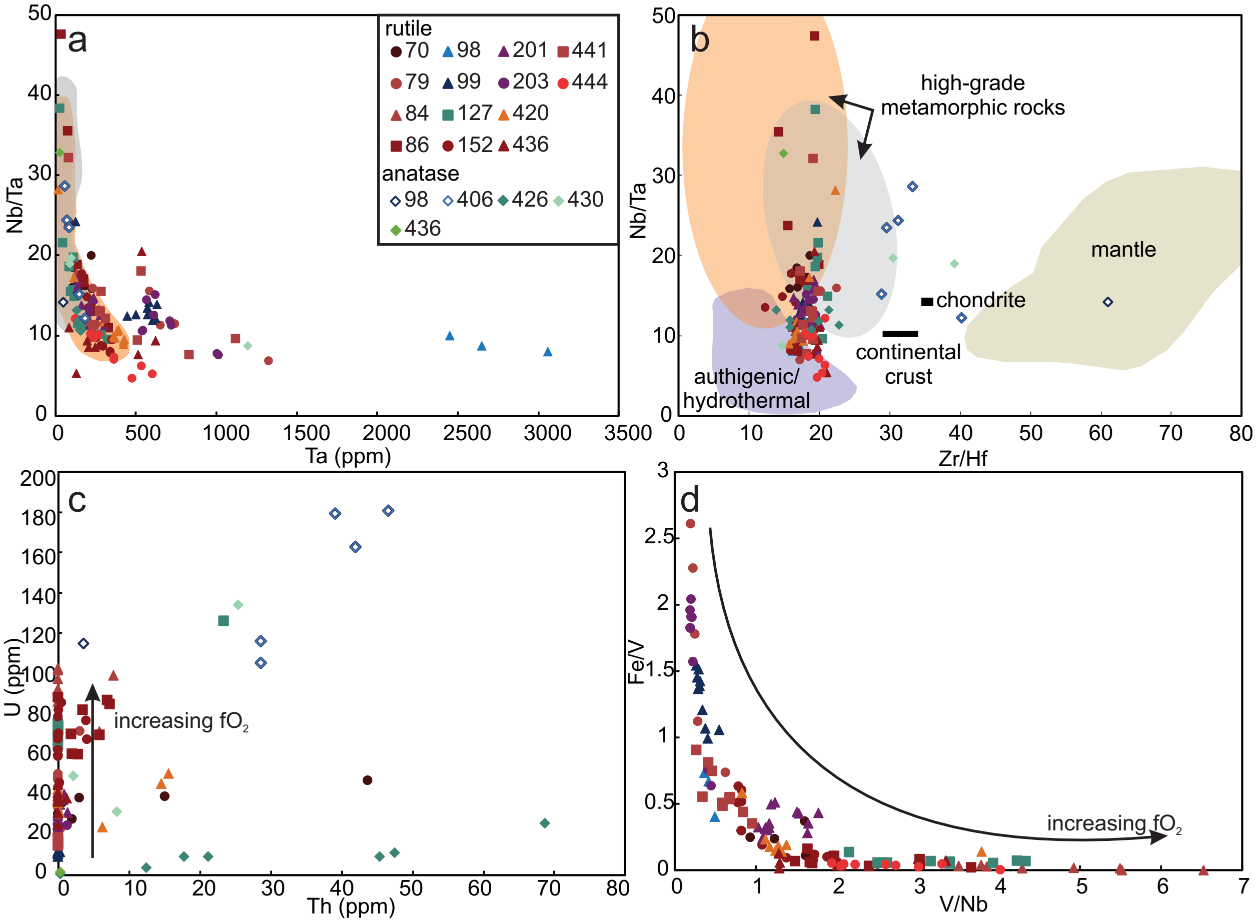
a
Nb/Ta
Ta (ppm)
0
10
20
30
40
50
0
500
1000
1500
2000
2500
3000
3500
rutile
● 70
▲ 98
▲ 201
■ 441
● 79
▲ 99
● 203
● 444
▲ 84
■ 127
▲ 420
■ 86
● 152
▲ 436
anatase
◇ 98
◇ 406
◆ 426
◆ 430
◆ 436
b
Nb/Ta
Zr/Hf
0
10
20
30
40
50
60
70
80
high-grade
metamorphic rocks
mantle
chondrite
continental
crust
authigenic/
hydrothermal
c
U (ppm)
Th (ppm)
0
20
40
60
80
100
120
140
160
180
200
increasing fO2
d
Fe/V
V/Nb
0
0.5
1
1.5
2
2.5
3
4
5
6
7
increasing fO2

Figure 9